



TECHNISCHE
UNIVERSITÄT
WIEN

Unterschrift BetreuerIn

DIPLOMARBEIT

**The Musician's Hand as a Bowing Parameter - Bowing
Pendulum Measurements and Finite Difference Modelling**

AUSGEFÜHRT AM
Institut für Angewandte Physik
Technische Universität Wien

IN ZUSAMMENARBEIT MIT DER
Fakultät DMI - Design, Medien, Information
Hochschule für Angewandte Wissenschaften Hamburg

unter der Anleitung von
Ao.Univ.-Prof. DI Dr.techn. Martin Gröschl
Prof. Dr. Robert Mores

EINGEREICHT AN
der Technischen Universität Wien
Fakultät für Physik

VON

Géza Horváth

Hans-Enzmann-Hof 1-12/6/4
A-3423 St. Andrä-Wördern

Acknowledgements

I am infinitely grateful to Robert Mores for his guidance and the generous opportunity to use his bowing pendulum.

Contents

1. Introduction	15
1.1. Scope and purpose of bowed string instrument research	15
1.2. Understanding playability and the player's bowing hand	16
1.3. Thesis structure	17
2. Bowing Pendulum Experiments to Investigate the Bowing Hand	19
2.1. Pendulum Setup	21
2.2. Data capturing and post processing	21
2.3. Results and discussion	25
2.3.1. Spectral centroid analysis	25
2.3.2. Signal power analysis	30
2.3.3. Power spectral density analysis (f_0, f_1)	31
2.4. Summary of findings	32
3. Finite Difference Numerical String Simulation	39
3.1. Physical model ingredients	39
3.1.1. Transversal string displacement	41
3.1.2. String torsion	42
3.1.3. Friction model	43
3.1.4. Bow hair, stick and player's hand	44
3.1.5. Bow driving mechanism	46
3.2. Model summary	46
3.3. Time-stepping algorithm	51
3.4. Simulation results	53
3.4.1. Average power and spectral centroid analysis	53
3.4.2. Partial slip, string torsion and bow hair vibrations	56
3.5. Summary of findings	60

4. Conclusions and Outlook	63
A. Scatter plots	67
A.1. Spectral centroid	67
B. Finite Difference Method Implementation	69
B.1. Equally Spaced Discretisation Grid	69
B.2. FD Equations	70
B.3. FD Operators	71
B.4. FD Model Equations	72
B.4.1. Slip	72
B.4.2. Stick	73
B.5. Matrix Notation	75
C. Q-factor and damping coefficients	77
D. Bibliography	79

List of Figures

2.1. Bowing pendulum schematics.	22
2.2. bow mounting	23
2.3. Single bow stroke example	24
2.4. Spectral centroid plots, $\beta \approx 1/14$	26
2.5. Spectral centroid at $F_n \approx 80$ g	27
2.6. $\beta \approx 1/14$, frequency spectrum envelopes	29
2.7. Spectral centroid plots, $\beta \approx 1/30$	33
2.8. Spectral centroid plots, $\beta \approx 1/30$	34
2.9. Signal power	35
2.10. Harmonic n_0 and n_1 relative power, $\beta \approx 1/14$	36
2.11. Harmonic n_0 and n_1 relative power, $\beta \approx 1/30$	37
2.12. Harmonic n_0 and n_1 relative power, $\beta \approx 1/9$	38
3.1. Classical friction curve $\mu(v_{rel})$	44
3.2. Horizontal polarisation bowing model	48
3.3. Vertical polarisation bowing model	49
3.4. Friction curve with numerical offset	51
3.5. Time-stepping algorithm workflow	52
3.6. Mean frequency and power	54
3.7. labelInTOC	55
3.8. Slip stick interaction, example 1, <i>piano</i>	57
3.9. Slip stick interaction, example 2, <i>forte</i>	57
3.10. Slip stick interaction, example 3	58
3.11. Slip stick interaction, example 4	59
3.12. Slip stick interaction, example 5	59
A.1. Spectral centroid scatter plot, $\beta \approx 1/14$	67
A.2. Spectral centroid scatter plot, $\beta \approx 1/30$	68

List of Figures

A.3. Spectral centroid scatter plot, $\beta \approx 1/9$ 68

List of Tables

- 3.1. Simulated state variables 46
- 3.2. Model parameters 50

List of Symbols

F_n	Normal bow force	g (equivalent mass)
v_b	bow speed	cm s^{-1}
β	relative distance from bridge	
F_f	friction force	N
$f_{restore}$	restoring force density acting on string	N m^{-1}
f_b	normal bow force density	N m^{-1}
v_{rel}	relative velocity between string and bow hair	m s^{-1}
$\mu(v_{rel})$	friction coefficient	
μ_s	static friction coefficient	
$f(v_{rel})$	distributed friction force	N m^{-1}
z	position along string	m
t	time	s
$\eta(z, t)$	transversal string displacement	m
$\chi(z, t)$	torsional string deflection	rad
$x_h(z, t)$	bow hair position	m
$x_b(t)$	bow stick position	m
$x_a(t)$	arm position	m
$\zeta(z, t)$	transversal string displacement	m
$y_b(t)$	bow stick position	m
$y_a(t)$	arm position	m
L	string length	m
T	string tension	N
B	bending stiffness	N m^2
m	linear mass density	kg m^{-1}
b_1	transversal damping coefficient	$\text{kg s}^{-1} \text{m}^{-1}$
b_2	transversal damping coefficient	kg m s^{-1}
K	torsional stiffness	N m^2

J	moment of inertia per unit length	kg m
a	string radius	m
d_1	torsional damping coefficient	kg m s^{-1}
k	foam spring constant	N m^{-1}
c	foam damping coefficient	kg s^{-1}
k_h	distributed bow hair spring constant	N m^{-2}
c_h	distributed bow hair damping coefficient	$\text{kg s}^{-1} \text{m}^{-1}$
m_b	bow stick mass	kg
m_a	arm mass	kg
m_g	driving mass	kg
w	driving unit impedance	kg s^{-1}
$c_{\text{transversal}}, c_{\text{torsional}}$	wave speed on string	m s^{-1}
$Z_{\text{transversal}}, Z_{\text{torsional}}$	string impedance	kg s^{-1}
ω	angular frequency	rad
Q_0	string quality factor at fundamental frequency	

Abstract

This work uses an existing precise bowing pendulum to measure the impact of the musician's bowing hand during sustained tones in the Helmholtz regime. An initial investigation by this author suggests that the flexibility of the player's hand influences the friction force between bow hair and string and the quality of sound produced. Current models of the bowed string, with the three playing parameters, normal bow force F_n , bow velocity v_b and relative distance to the bridge β , do not include this effect. In order to emulate a relaxed bowing hand, the bow was mounted to the bowing pendulum with the help of soft foam, alternative to a more rigid, leather-cladded mounting. The change in mounting audibly influences the sound produced on a cello's open G string. In particular, the spectral centroid is shifted to lower or higher frequencies and energy is absorbed differently by the vibrating bow, depending on the three playing parameters. This work combines multiple physics based models of the bowed string available in literature, in a numeric finite difference implementation. It succeeds in describing partial slipping phenomena during the Helmholtz motion, related to torsional motion. Furthermore it suggests, that refined models should include coupling between transversal string displacement polarisations and a detailed model of bow hair and stick modes, in order to reproduce the bowing pendulum findings. This is a step towards understanding the playability and sound reproduction of bowed instruments, which is of interest to string and bow makers, luthiers and players/teachers alike.

Kurzfassung

In dieser Arbeit wurden mit einem präzisen Bogenpendel die Auswirkungen der Bogenhand, während ausgehaltener Töne im Bereich der Helmholtzschwingungen, gemessen. Eine Voruntersuchung durch den Author suggeriert, dass die Flexibilität der Hand eines Musikers, die Reibungskräfte zwischen Bogenhaaren und Saite, als auch die Klangqualität beeinflusst. Aktuelle Modelle der gestrichenen Saite, mit den drei Spielparametern, normale Bogenkraft F_n , Bogengeschwindigkeit v_b und relative Distanz zum Steg β , beschreiben diesen Effekt nicht. Um eine entspannte Bogenhand zu emulieren, wurde der Bogen mit weichem Schaumstoff am Bogenpendel befestigt, alternativ zu einer festeren, lederummantelten Befestigung. Die unterschiedliche Bogenbefestigung beeinflusst den Klang einer leeren Cello G Saite hörbar. Insbesondere wird der spektrale Zentroid zu tieferen und höheren Frequenzen verschoben, abhängig von den drei Spielparametern. Diese Arbeit kombiniert mehrere, in der Literatur verfügbare, Physik basierte Modelle der gestrichenen Saite, in einer Implementierung der numerischen Finite-Differenzen-Methode. Das Modell beschreibt erfolgreich die mit der Torsionsbewegung zusammenhängenden Phänomene des Teilabrutschens während der Helmholtzschwingung. Außerdem legt es nahe, dass künftige verbesserte Modelle eine Kopplung zwischen den Polarisationen der transversalen Auslenkung der Saite, sowie eine detaillierte Modellierung der Bogenhaar und -stangen Moden berücksichtigen sollten. Dies ist ein Schritt in Richtung verbesserten Verständnisses der Spielbarkeit und Klangproduktion von Streichinstrumenten, was für Geigenbauer, Bogenbauer, Saitenhersteller und Musiker sowie Lehrer von Interesse ist.

Chapter 1.

Introduction

1.1. Scope and purpose of bowed string instrument research

The violin family instruments' design remains unchanged for more than 300 years and their quality has reached a level of refinement which seems unsurpassable. Both were achieved empirically by honing craftsmanship skills and passing them down from generation to generation. Insofar the scientific method cannot aspire to improve anything of major significance. It would be unclear, what the definition of "improve" might be, as musical acoustics contains a strong component of personal taste and preference. The listener's expectations and instrument design have always evolved concurrently and any radical change would be met with great scepticism.

Certainly the musical instrument can be analyzed as a physical body in the same way that music can be investigated concerning its acoustical material. However the effect of music in its spiritual idea and the effect of the instrument's sound and timbre in its aesthetic idea can only be realized by one who is willing to sharpen his musical awareness by learning to listen. (M. Schleske)

Luthier Martin Schleske uses an approach of making *tonal copies* [1]. He investigated how changes to the top and bottom plates of a violin effect specific changes in vibrational mode patterns. Armed with this knowledge he replicates the resonance spectra of existing violins with remarkable success.

His approach of understanding certain physical effects and properties of an instrument's body and manipulate them for a desired effect can certainly be applied to the bow and string interaction and the question of playability.

As with most fundamental research, curiosity is a major drive. While we do not expect to find any new physical effects, the hope of understanding and quantifying the processes of bowed string instruments, on par with the level of detail and accuracy the marvelous mechanism of human hearing provides, represents a strong reward.

1.2. Understanding playability and the player's bowing hand

We can observe various styles of successful playing technique, all leading to a remarkable, musical sound. While cellist Lynn Harrell advocates leaning ones torso slightly forward, to increase the natural weight of the arm acting on the bow, Yo-Yo Ma is well known for leaning backwards. Sol Gabetta performs with an, at times awkwardly raised, seemingly tight right shoulder and yet she has a successful career as a soloist and teacher. The human anatomy is diverse and so are the finer details of the bow grips of professional musicians. Certainly, there is no *right* way to play, although there are basic movements and techniques that obviously work, while others do not. To systematically understand playability, identifying some common features of great performance and their particular influence on sound production, seems to be a good approach.

Current models of the bowed string consider three major bowing parameters. The normal force F_n acting on the string, bowing velocity v_b , and relative distance β from the bridge. Researchers have constructed various mechanical bowing devices to measure the response of stringed instruments with precise control of these parameters. More detailed finite bow width models have also considered a varying bow width as a result of a tilted bow. Unfortunately we still lack in detailed understanding of what musicians do, to achieve a particular set of parameters and a distinguished sound.

Teachers tell their students early on, not to press the bow onto the string. Instead, players should relax their arm and let arm and bow fall onto the string freely. A sensor measuring F_n cannot distinguish the former from the latter, and yet, any trained musician will immediately recognize players with a strong bow grip trying to press the bow onto the string. While

superior in accuracy and repeatability, bowing machines with high mechanical impedance electric motors remain similar to tight bow grip players, rather than an accomplished musician with precise muscle control, where fingers, wrist, arm and even torso all work in accord.

The hand is a good indicator of skilled bowing technique and many bowing exercises target the fingers and wrist in particular. It seems reasonable to include the player's hand in an improved model of bowing. As a starting point for this work, we think of the hand's role as some flexible coupling between the bow and the mass of the arm.

1.3. Thesis structure

This thesis consists of two major parts. First, Chapter 2 presents results of a measurement session with a precise bowing pendulum, developed by R. Mores [2]. The bow was attached to the pendulum either with flexible foam around frog and tip, or with a more rigid leather-cladded bow mounting, to immitate a relaxed or tight bow grip. An investigation of steady Helmholtz motion targets possible differences in bowing parameters and sound radiated, between both cases.

Second, Chapter 3 gathers the physical bowing models available in literature, combines them and adds a relaxed hand model inspired by the bowing pendulum setup. Numerical finite difference simulation results are presented in an attempt to verify the model and compare results from bowing pendulum experiments.

Chapter 2.

Bowing Pendulum Experiments to Investigate the Bowing Hand

This work uses a precise bowing pendulum developed by Mores [3], where the frog of the bow was wrapped in foam to crudely imitate a relaxed bowing hand, allowing vibrations of the bow. Measurements across the normal playing parameter space and comparison of the foam-wrapped bow with a more rigid, leather-cladded bow mounting (*free* and *rigid* bow mounting) show clear differences in tonal quality, particularly with the mean frequency (or spectral centroid) metric as a robust predictor of perceived “brightness”.

A number of researchers have developed mechanical bowing devices. Repeatability of bowing gestures to a higher degree of accuracy and reliability than humans could, forms a staple of systematic bowed string research. Early work by Raman in 1920 [4] held the bow in place and instead moved the violin on a sledge-like device. He recognized the importance of the bow mounting, using a balanced lever rotating on ball bearings to control the bow force.

The bow is held carefully balanced in the fingers of the right hand, the necessary increases or decreases in the pressure of bowing being brought about by increase or decrease of the leverage of the fingers. The suppleness of the wrist of the player and the flaccidity of the muscles of the forearm secures the necessary smoothness of touch. (C.V. Raman)

Later, Kar et al. [5] used a more elaborate design, with the bow mounted to a moving metal rod and a violin suspended below by long springs to adjust and measure bowing pressure.

A different approach was used by Lawergren [6], attaching the bow to wagons running along tracks and controlling the bowing pressure by placing the violin on a screw jack below. In a similar arrangement, Pickering [7] pressed the bow against the string with a weighted wheel.

Cronhjort [8] clamped a bow to a PC-controlled carriage of a daisy wheel printer. He controlled the bow force by applying torque via a motor-driven cantilever. Schoonderwaldt et al. [9] used this arrangement for bow force limit investigations.

Vogl in collaboration with string manufacturer *Thomastik Infeld*, Vienna [10], built a device for quality control purposes, where a sledge is driven along a linear axis and the bow is mounted on a lever system attached to the sledge.

The more recent work by Galluzzo and Woodhouse [11], in similar fashion, uses a linearly driven carriage. They clamped the bow to a leaf spring to apply torque and control the bow force with the help of an electromagnetic shaker. Their additional efforts with open-loop feedback control, offer gestural input control with greater precision.

All these well-thought-out mechanical bowing devices use an electric motor to drive the bow and control the bowing velocity. Their common approach is to understand bowing gestures in terms of the three major parameters F_n , v_b and β and to reproduce them as accurate as possible. The high mechanical impedance electrical motors and rather rigid bow mountings force the bow on a strict path. Electric motors do not “feel” the interaction physics of the string and bow hair contact area, they cannot adapt on the fly.

Unfortunately, this is at odds with how a musician would approach bowing, as they constantly adapt to the feedback they receive from bow and instrument. As Raman noted, musicians are very much concerned with smoothness of touch. We should think of bowing as “lettings things happen” just within the constraints of a gently guiding hand and arm.

Your wrist should move on an axis perpendicular to the string and think of the edge of your wrist pushing [in bowing direction] against an imaginary resistance. All your fingers should have contact with the bow stick and try to have an even distribution of force. Your thumb joints should be bent and relaxed.
(J. Kubitschek, cellist and teacher)

The bowing pendulum used with this research is much closer to this interpretation of bowing. Its design and properties are discussed in the following section.

2.1. Pendulum Setup

A cello's open G string was bowed and measured with a precise bowing pendulum (Figure 2.1) and measuring instruments as described in [3]. Key features include:

- Mass M_1 , emulating the player's arm, moves horizontally.
- Bow force F_n is precisely adjustable through the length of screws at b and c, thereby lowering or raising mass M_2 .
- Mass M_2 and its damping device (consisting of a mass dropping into water) with low mechanical impedance, determine the bowing speed by reacting to the friction force F_f . This is a much closer approximation of a musician's bowing, than a high mechanical impedance electric motor.
- Sensors S_1 , S_2 and S_3 measure the playing parameters v_b , friction force and F_n .
- The pendulum's bowing direction is self-stabilising, maintaining a constant bow hair to bridge distance, with less than 0.5 mm variation.

Experiments were conducted on a "teacher level" cello, crafted by *Laberte-Humbert Frères, Mirecourt*, in 1926. And a German bow by *Emil Werner*, reasonably coated with rosin, as a musician would during normal play. Bow hair tension was adjusted to a level suitable for normal play. The string measured, was a tungsten wound *Spirocore* G string by *Thomastik-Infeld*, Vienna. The cello rests horizontally on supports at the end pin and neck and is backed by wooden rests at the ribs, to prevent it from rotating. This resembles a player's hold of the instrument and limits any effects on the vibrational modes of the instrument's body.

Figure 2.2 depicts the free and rigid bow mountings. The foam-wrapped bow mounting is designed in such a way, that the bow is almost dropping due to its own weight, resembling a light bow grip.

2.2. Data capturing and post processing

Each bow stroke was captured with two force sensors (normal bowing force and tractive force), a horizontal bow position sensor, a microphone placed 1 m from the bridge and a

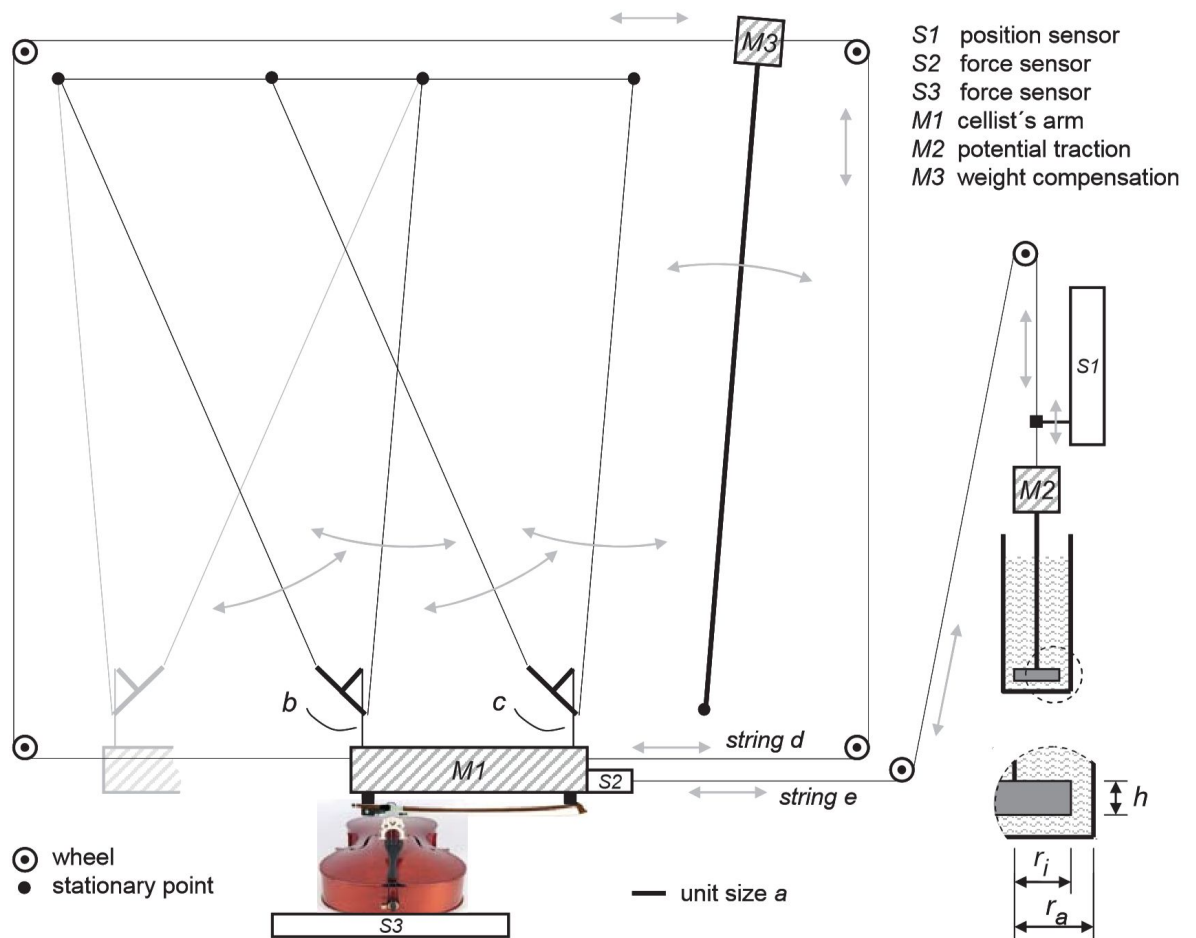


Figure 2.1.: Bowing pendulum schematics. Due to excentric mounting brackets, mass M_1 moves horizontally. With a carefully adjusted counter mass M_3 and a disconnected string e , M_1 stays at rest at every position

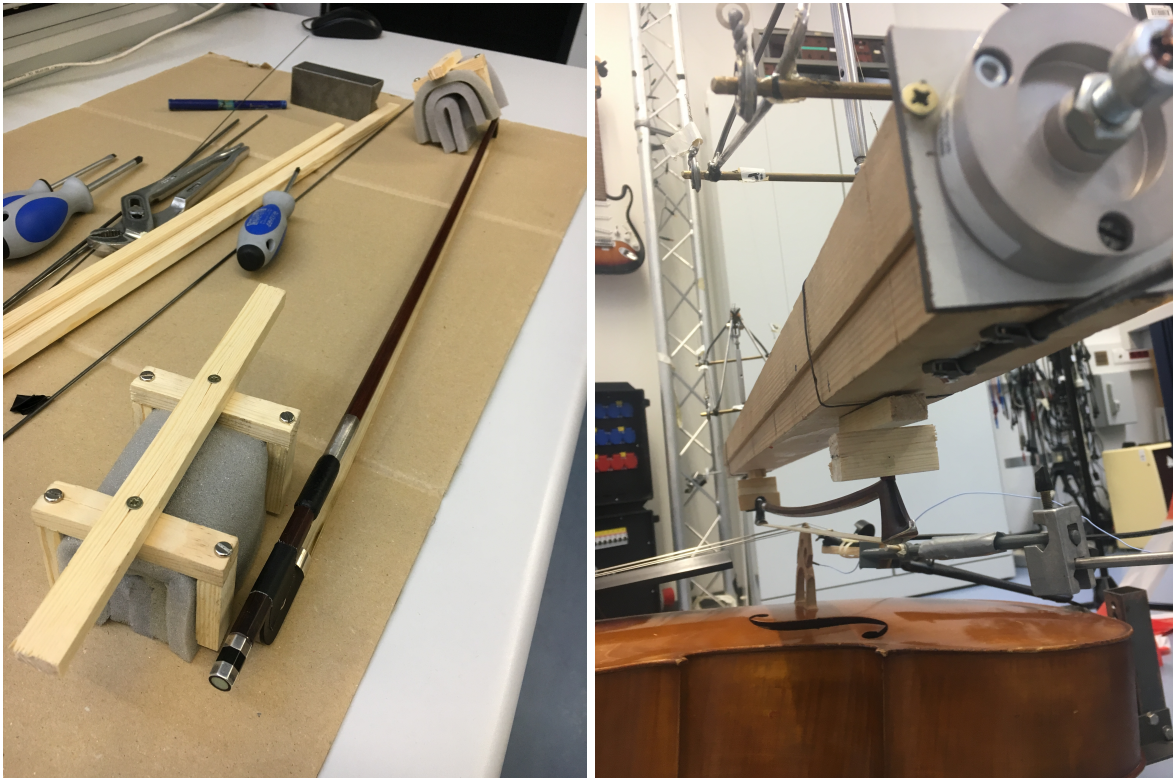


Figure 2.2.: Foam-wrapped bow mounting (left) and rigid, leather-clad bow mounting (right).

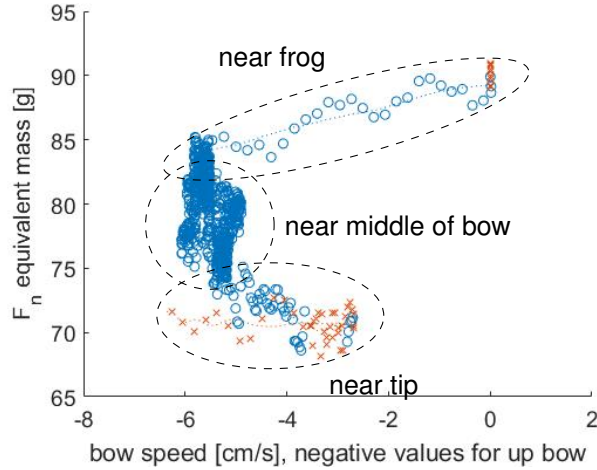


Figure 2.3.: An example of a single bow stroke. Each marker corresponds to a signal averaged over 10 ms, blue circles indicate Helmholtz motion, red crosses non-Helmholtz motion. Recorded with $\beta \approx 1/14$.

piezo sensor attached to the bridge. Bowing velocity and acceleration are derived from the horizontal bow position sensor.

Despite careful adjustment of the counter pendulum with mass M_3 , the bowing pendulum's damping forces are not entirely uniform across all bow positions. Also a tradeoff between the tension in string d and the friction forces at the wheels is necessary. All damping forces, depending on bow position, were measured with dry runs, without any string contact. When, additionally, accounting for inertial forces, the friction force between bow hair and string F_f was extracted from sensor S_2 's data, according to Equation (2.1).

$$F_f = F_{S_2} - F_{inertial} - F_{damping} \quad (2.1)$$

Figure 2.3 shows typical data for F_n and v_b recorded from a single up-bow stroke. A YIN-algorithm [12] performed classification of Helmholtz and non-Helmholtz motion from the bridge-mounted piezo's signal. As this is an analysis of steady Helmholtz motion.

As this is an analysis of steady Helmholtz motion, microphone recorded sound samples should preferably show as little variation in F_n and v_b as possible, while data from transients near tip and frog should be excluded. Non-Helmholtz motion data tuples were discarded, while the remaining data tuples were grouped into segments, 0.34 s in length with 75% overlap. A classic short-time Fourier transform on the microphone signal, with a Blackman

window 16384 samples in length (0.34 s at 48 kHz), prepares spectral analysis. Segments whose F_n and v_b averages have standard deviations $\sigma(F_n) > 3\text{ g}$ or $\sigma(v_b) > 0.3\text{ cm s}^{-1}$ are discarded. To summarize, this leaves us with many steady Helmholtz motion 0.34 s sound samples, their associated frequency spectra and their respective average values of F_n and v_b with little variation.

2.3. Results and discussion

To extract the possible impact of a relaxed bowing hand, this research attempted to cover as wide a range of normal playing parameters (F_n, v_b, β) , where steady Helmholtz motion occurs, as possible. Comparing a free and rigid bow mounting, exhibits clearly audible differences. Visualised to some extent with the spectral centroid (Section 2.3.1) as a robust metric for perceived brightness [13] and an analysis of the power spectral density (Section 2.3.3) with a focus on the first few harmonic frequencies.

Results are presented as gridded pseudocolour plots on the parameter space spanned by F_n and v_b , measured at three distinct values of β (1/9, 1/14 and 1/30). Alas, due to measuring time constraints, a more exhaustive search of the parameter space was not possible. Each coloured grid square represents an average of the underlying data points (each data point representing a 0.34 s steady Helmholtz motion sound sample and its associated sensor data), allowing an easy comparison between the free and rigid bow mounting. Please refer to Appendix A for the scatter plots of the underlying data points.

2.3.1. Spectral centroid analysis

The spectral centroid can be understood as the ‘‘center of mass’’ of a given frequency spectrum $x(n)$, with center frequency $f(n)$ of bin number n and is defined as

$$\text{centroid} = \frac{\sum_{n=0}^{N-1} x(n)f(n)}{\sum_{n=0}^{N-1} x(n)}. \quad (2.2)$$

Medium β . Figure 2.4 shows the spectral centroid on the F_n and v_b parameter space of 107 up-bow strokes at $\beta \approx 1/14$, chosen as an intermediate value, from experience with the

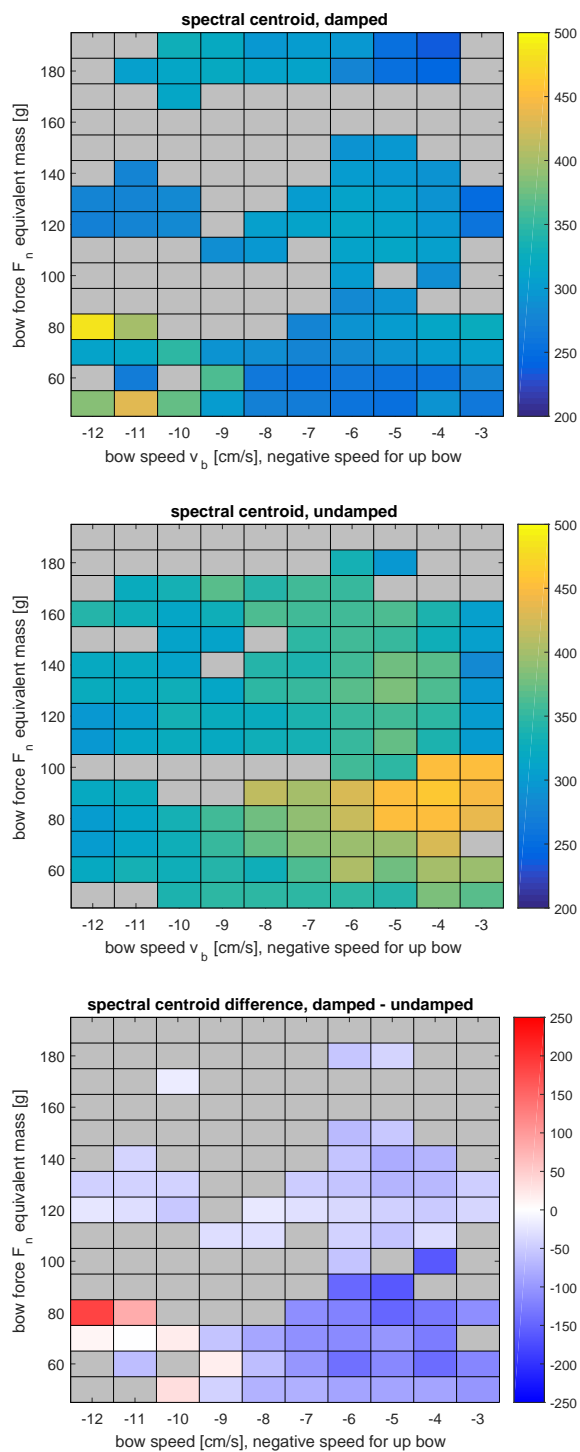


Figure 2.4.: $\beta \approx 1/14$, spectral centroid parameter space analysis. Free (top), rigid (middle) bow mounting and difference between both cases (bottom).

cello. Adjusting the driving mechanism's mass M_2 , lead to varying bow speeds, depending on the bow force. Results from free and rigid bow mounting and the difference between both cases, are presented as spectral centroid pseudocolour plots, analysed from sound recorded with a microphone placed 1 m from the bridge. Grey rectangles indicate no available steady Helmholtz motion data. The fundamental frequency of the open G string was tuned to 98 Hz.

In both cases, free and rigid bow mounting, there is a trend of a spectral centroid maximum at lower v_b , gradually shifted to higher v_b with increasing F_n . The largest maximum occurs with an rigid bow mounting at a low bow speed of -4 cm s^{-1} and low bow force equivalent mass of 85 g. At $\beta \approx 1/14$, a foam wrapped bow mounting generally lowers the spectral centroid, with the exception of high bow speeds and low bow force.

Above 120 g bow force equivalent mass, the spectral centroid shows a relatively uniform distribution. Data indicates a general trend of a decreased spectral centroid at higher and very low bow speeds, with a maximum in between and the undamped case's maximum being more pronounced. The free case shows a lower spectral centroid, by approximately 50 Hz.

There are no data points at high bow force and very low bow speeds. Since the pendulum is gravity driven and no particular bow speed is forced, the bow tends to stick below a certain speed threshold and no steady Helmholtz motion occurs.

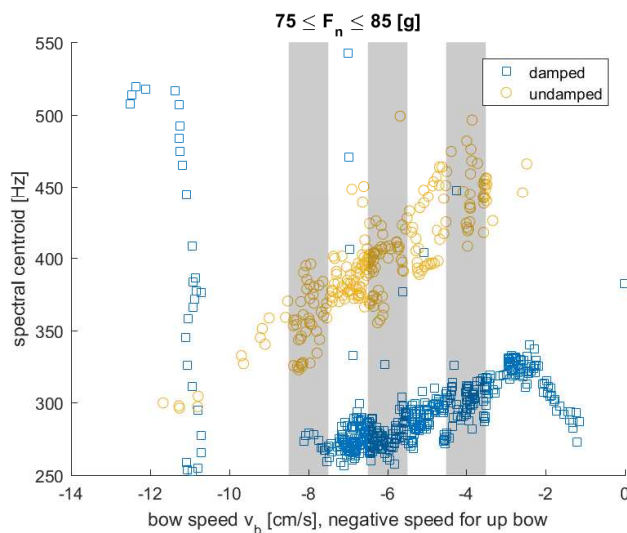


Figure 2.5.: Spectral centroid analysis at $\beta \approx 1/14$ and 80 g F_n equivalent mass, corresponding to an as free as possible suspension of the bow above the string.

Remarkably, the most significant differences occur right around a bow force corresponding to the bow's own mass of 80 g. In the foam-wrapped case, this would correspond to a relaxed playing state, where the musician holds the weight of his own arm and grips the bow as lightly as possible. For a closer investigation, Figure 2.5 presents the spectral centroid of all sound samples in the F_n range from 75 to 85 g. The separation in spectral centroid and different dependence on v_b between the free and rigid case, is immediately apparent. The free bow mounting exhibits a few outliers with high spectral centroid.

The outliers at high v_b are attributed to two particular bow strokes and are associated with a flagolet-like sound. This can be explained as a result of the limited capability of the fundamental frequency estimating YIN algorithm to classify Helmholtz motion from the bridge mounted piezo sensor. A definitive classification would require a look at the precise translational displacement at the bowing contact surface, to reliably identify even slight double slipping. These outliers occur near the minimum bow force, most likely right at the boundary, where differential slipping crosses into the double slipping non-Helmholtz motion regime. The rigid bow mounting shows no such outliers. Possibly there is a bow mounting dependent effect at play, related to partial slipping, requiring further investigation.

To illustrate the changing sound more precisely, Figure 2.6, depicts the average power spectral density envelope of all sound samples in the respective shaded areas of Figure 2.5. The spectral centroid is mostly influenced by the first five to ten harmonics. Most of clearly audible differences occur within the first four harmonics. Generally, all spectra show similar features, the sound was radiated from the same instrument. Nevertheless, a number of differences can be associated with changes in bow mounting and bow speed.

The free bow mounting's second and third harmonic are lowered by more than 10 dB, while the fundamental frequency is slightly more powerful than with a rigid bow mounting. The stronger shift to a higher spectral centroid with slower bow speeds and a rigid bow mounting — as indicated by the dashed lines — is primarily caused by shift in power towards the third and fourth harmonic. At the slowest bow speeds, the fourth harmonic radiates the most power, a significant difference when compared to the free bow mounting, where the fundamental frequency consistently dominates in radiated power. This free power spectral density envelope exposes dips in power relative to the rigid spectrum at a number of harmonics, particularly at the 2nd, 3rd, 7th, 16th, 17th and 23rd harmonic.

Furthermore, the rigid sound signal consistently contains more power, it is audibly louder. Section 2.3.2 provides further analysis on signal power.

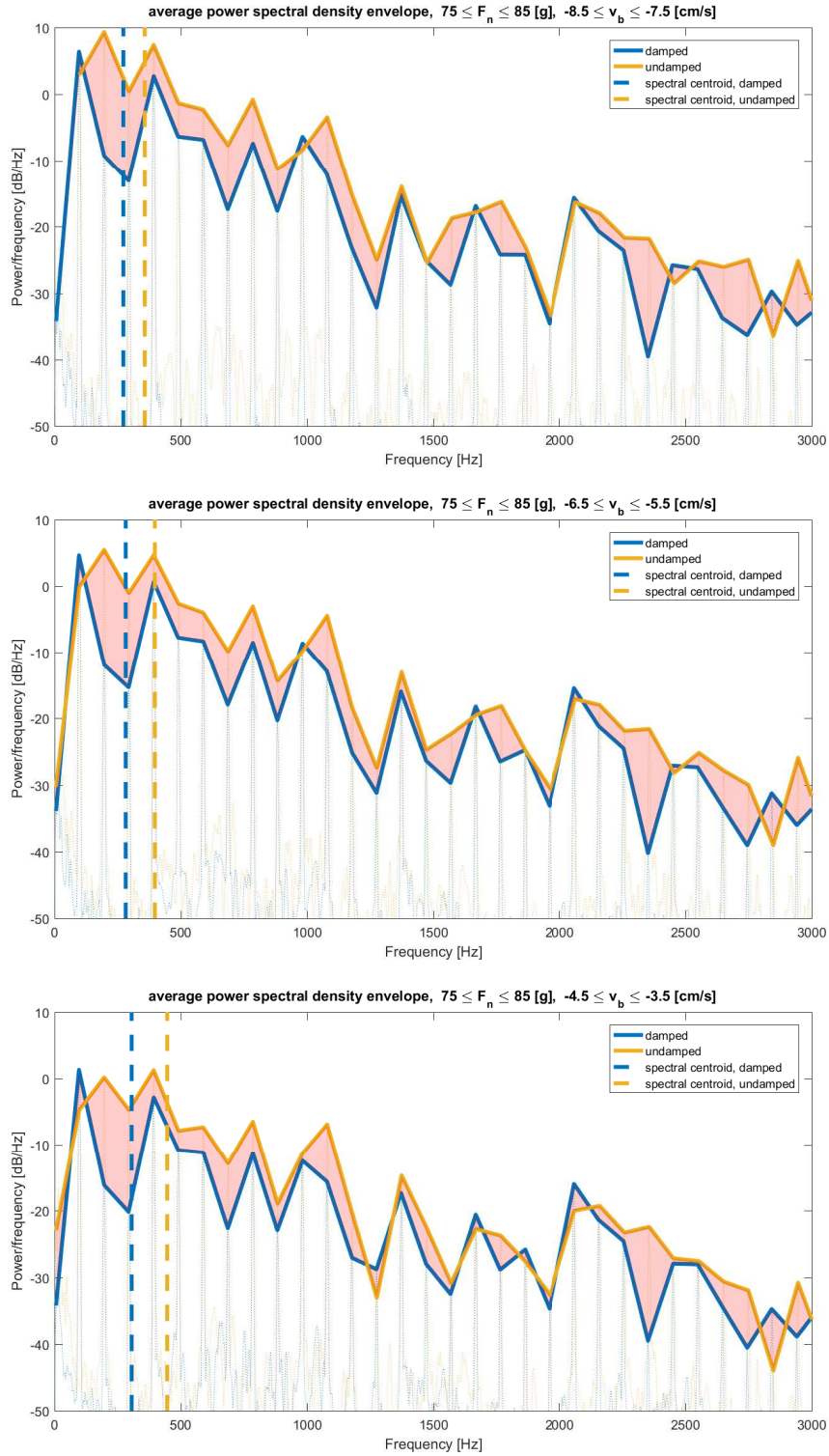


Figure 2.6.: $\beta \approx 1/14$, average frequency spectrum envelope over all sound samples in the respective shaded area in Figure 2.5. Recorded near 80 g F_n equivalent mass, corresponding to the bow's own mass.

Small β . Figure 2.7 shows the parameter space of 104 up-bow strokes at $\beta \approx 1/30$. Musicians often use this area close to the bridge with a bow force on the higher end of the spectrum, during musical passages in *forte*, requiring an intense, brilliant sound.

As Schelleng observed in his diagram [14], the playing parameter space leading to Helmholtz motion is increasingly constricted at lower β . The results presented here replicate this, as no Helmholtz motion occurs at low bow force and higher bow speed. A higher bow force is required to drive Helmholtz motion at higher bow speeds, the results presented in 2.7 were obtained around the minimum bow force. The minimum bow force limit was recently investigated by Mores [15], using this bowing pendulum. Instead, changes in spectral centroid during steady Helmholtz motion were explored here and more data points would be needed for an analysis of transients.

Close to the minimum bow force, the spectral centroid is shifted to higher frequencies with a free bow mounting. Consistent with the results from medium β in Figure 2.4, the spectral centroid is shifted to lower frequencies with a free bow mounting, when moving away from the minimum bow force limit, towards slower bow speed and higher bow force in the upper right corner of the parameter space. The medium β results provide a hint of this spectral centroid shift reversal near the lower bow force limit. No significantly different behaviour emerges near a F_n equivalent mass equal to the bow's own mass of 80 g.

Large β . Figure 2.8a shows the parameter space of 85 up-bow strokes at $\beta \approx 1/9$. On the particular cello measured, this is just above the fingerboard, an area that offers a different, softer sound, often used in piano passages, particularly in orchestral play.

The spectral centroid varies very little across the parameter space, when compared to smaller β . Generally, the free bow mounting shifts the spectral centroid to higher frequencies by 60 Hz on average, in opposition to the shift towards lower frequencies at medium β . Again, this is a significant, clearly perceivable when listening to the recorded sound samples. As with small β , no distinctly different behaviour emerges near a F_n equivalent mass equal to the bow's own mass of 80 g.

2.3.2. Signal power analysis

Medium and high β . The middle and right column in Figure 2.9 shows the power of the microphone signal (20-10 000 Hz band) across the playing parameter space from the same

sound samples used in spectral centroid analysis in the previous section. Radiated sound power depends on bow velocity and not on bow force, again in accordance with Schelleng's results [14]. Bowing closer to the bridge generally leads to a higher sound level. Using the same bowing parameters, the rigid bow mounting produces an audibly louder sound, with differences up to 10 dB between the rigid and free case, at low F_n and higher v_b .

Small β , depicted in the left column of Figure 2.9. Closer to the minimum bow force near the bridge, signal power behaviour is more complex. The clear dependence on bow velocity is only observed at F_n equivalent mass of 120 g or higher. As expected, the loudest sound sample was recorded near the bridge at high bow velocity and, remarkably, with a rigid bow mounting. A musician's analogous playing state could be described as playing with great force, transmitted through a tight bow grip. A free bow mounting exhibits a maximum in signal power at high bow force and *low* bow speed, strikingly with increased power over the rigid bow mounting in the same parameter space are. These measurements suggest the presence of a sweet spot when playing *forte* with a relaxed bowing hand near the bridge. When comparing the spectral centroid in Figure 2.7 across the same parameter space, high sound power seems to be associated with a spectral centroid shift towards lower frequencies. However, it remains unclear what precise mechanism could cause this.

2.3.3. Power spectral density analysis (f_0, f_1)

The previous sections established the first few harmonics' major influence on spectral centroid and radiated sound level. The following investigates the relative power contained in the fundamental frequency (f_0) and the first harmonic (f_1), across the previously established playing parameter space. Again, results are presented at the three distinct values of β in Figures 2.10 to 2.12. f_0 's power relative to the entire signal is shown in the left column of each figure (free, rigid and difference), while the columns on the right depict f_1 's relative power.

Medium β , Figure 2.10. With a free bow mounting, the fundamental frequency contributes more to the entire signal, consistently across the playing parameter space measured. The first harmonic exhibits the opposite behaviour, with a rigid bow mounting, its contribution increases. Around the bow force equivalent weight of 80 g, this pattern emerges more clearly.

Small β , Figure 2.11. Differences between bow mountings are generally smaller, except at high F_n and v_b , where a rigid bow mounting leads to the first harmonic dominating the power

spectral density. Remarkably, with both bow mounting, the first harmonic increases in relative power at high F_n and low v_b .

Large β , Figure 2.12. Closer to the bridge, relative power content generally varies less across the parameter space, consistent with previous plots. As with medium β , the free bow mounting shifts power to the fundamental frequency, although to a smaller degree and without any noticeable pattern around F_n corresponding to the bow's own weight.

2.4. Summary of findings

A free, foam wrapped bow mounting (corresponding to a relaxed bowing hand) and rigid, leather-cladded bow mounting (tight bowing hand) affect a cello's sound radiation in different ways, depending on bowing parameters F_n , v_b and β . Spectral centroid, average power and power spectral density all exhibit bow mounting dependent variations.

At medium β , a free bow mounting generally shifts the spectral centroid to lower frequencies, while the opposite is the case close to the bridge and close to the fingerboard. Remarkable patterns can occur around a bow force equivalent to the bow's own weight, suggesting an involvement of the bow stick's properties.

With a free bow mounting, radiated sound power is lowered at most parameter combinations, strongly suggesting that the vibrating bow stick absorbs energy.

Changes in power spectral density of the radiated sound were precisely quantified, with particularly significant effects within the first few harmonic frequencies, providing additional empirical data for model verification purposes.

The empirical results presented here, clearly show, that two strokes with identical playing parameters F_n , v_b and β can produce, during sustained Helmholtz motion, significantly audible sound differences, as supported by spectral analysis. An improved bowing model requires at least one additional parameter, describing the strength of vibration of the bow stick.

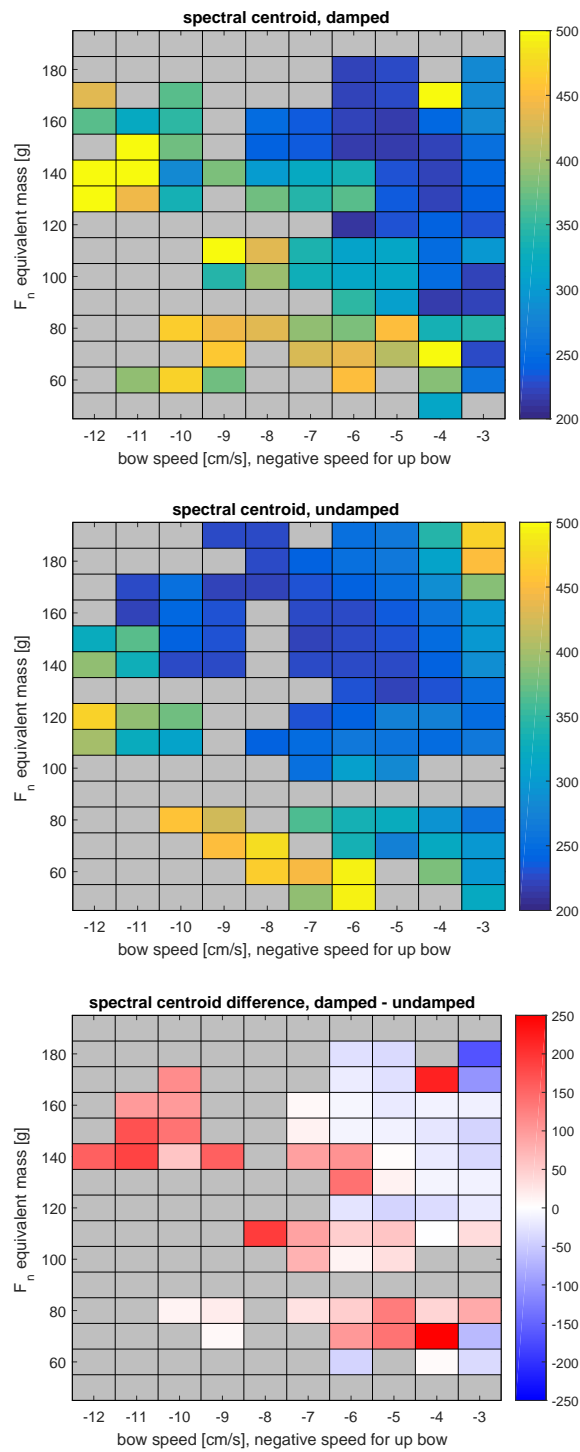


Figure 2.7.: $\beta \approx 1/30$, spectral centroid parameter space analysis. Free (top), rigid (middle) and difference between both cases (bottom).

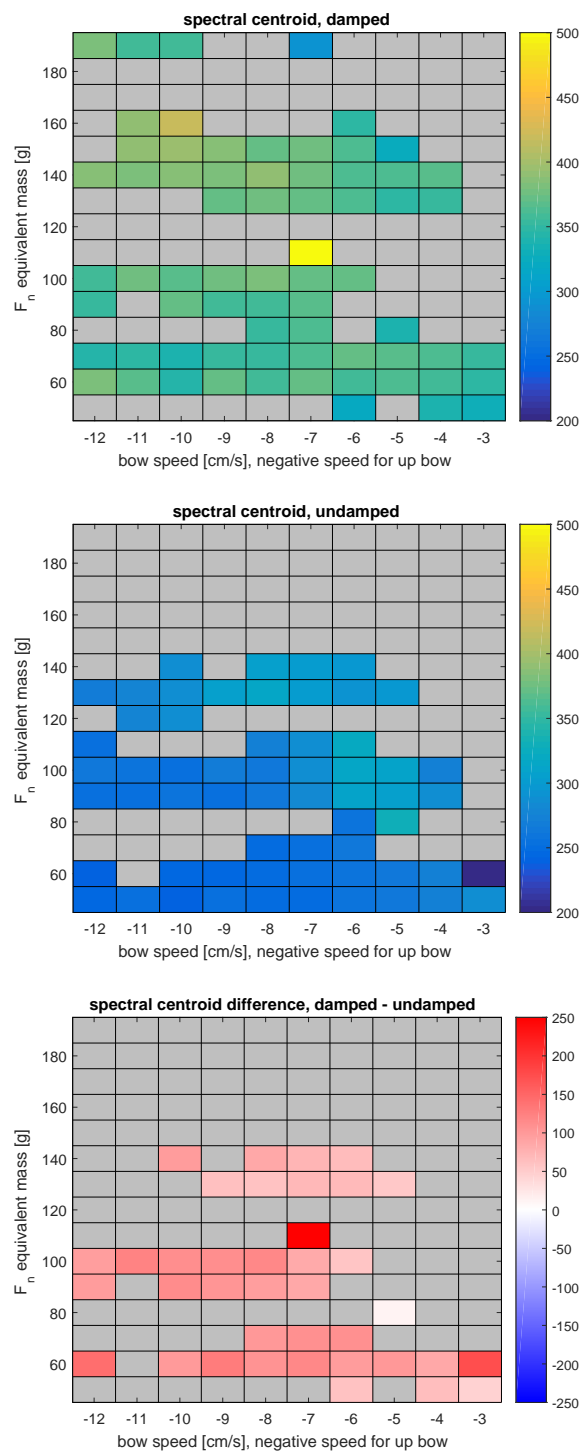


Figure 2.8.: $\beta \approx 1/9$, spectral centroid parameter space analysis. Free (top), rigid (middle) and difference between both cases (bottom).

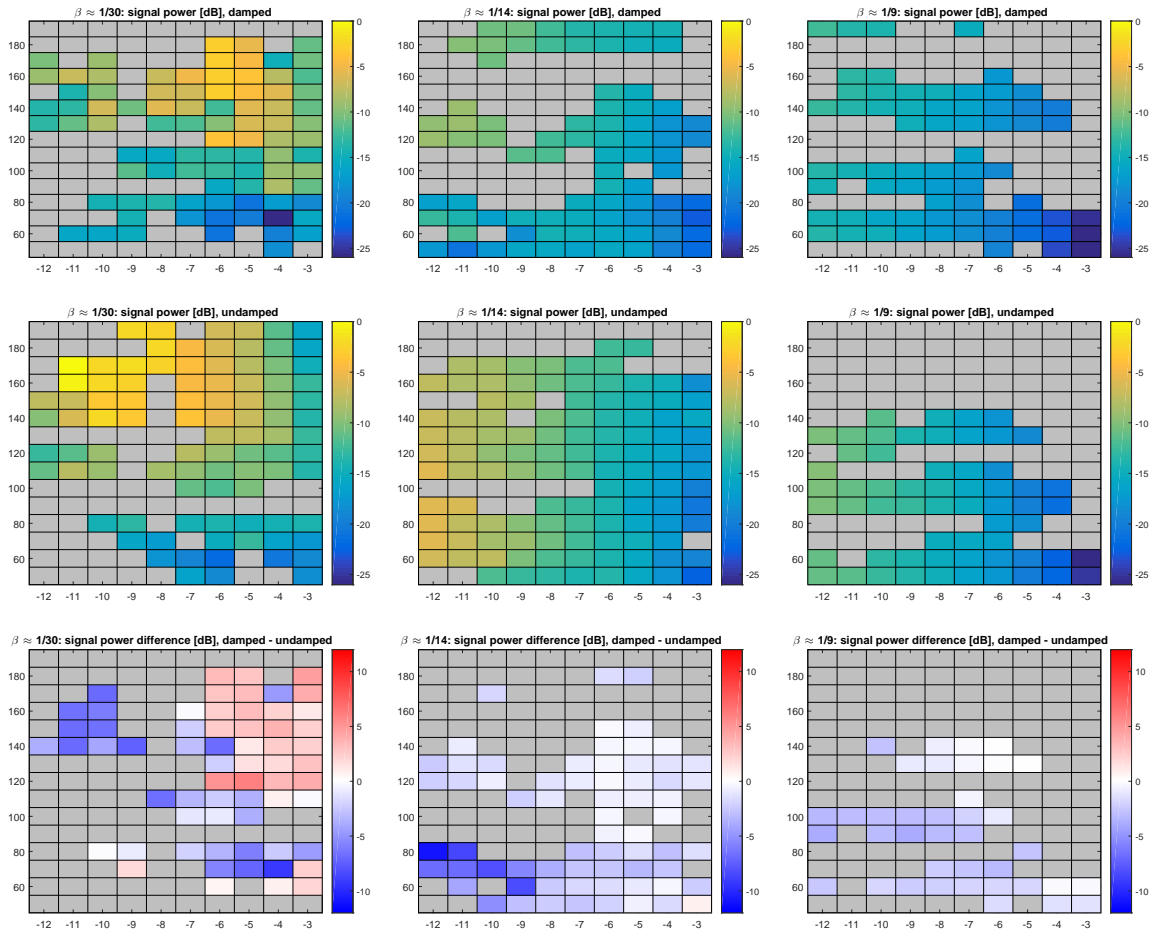


Figure 2.9.: Power of the microphone signal in the 20-10000 Hz band, relative to the loudest sample recorded. The abscissa defines the bow speed v_b in [cm/s] with negative speeds for up-bow, while the ordinate defines the bow force F_n equivalent mass in [g].

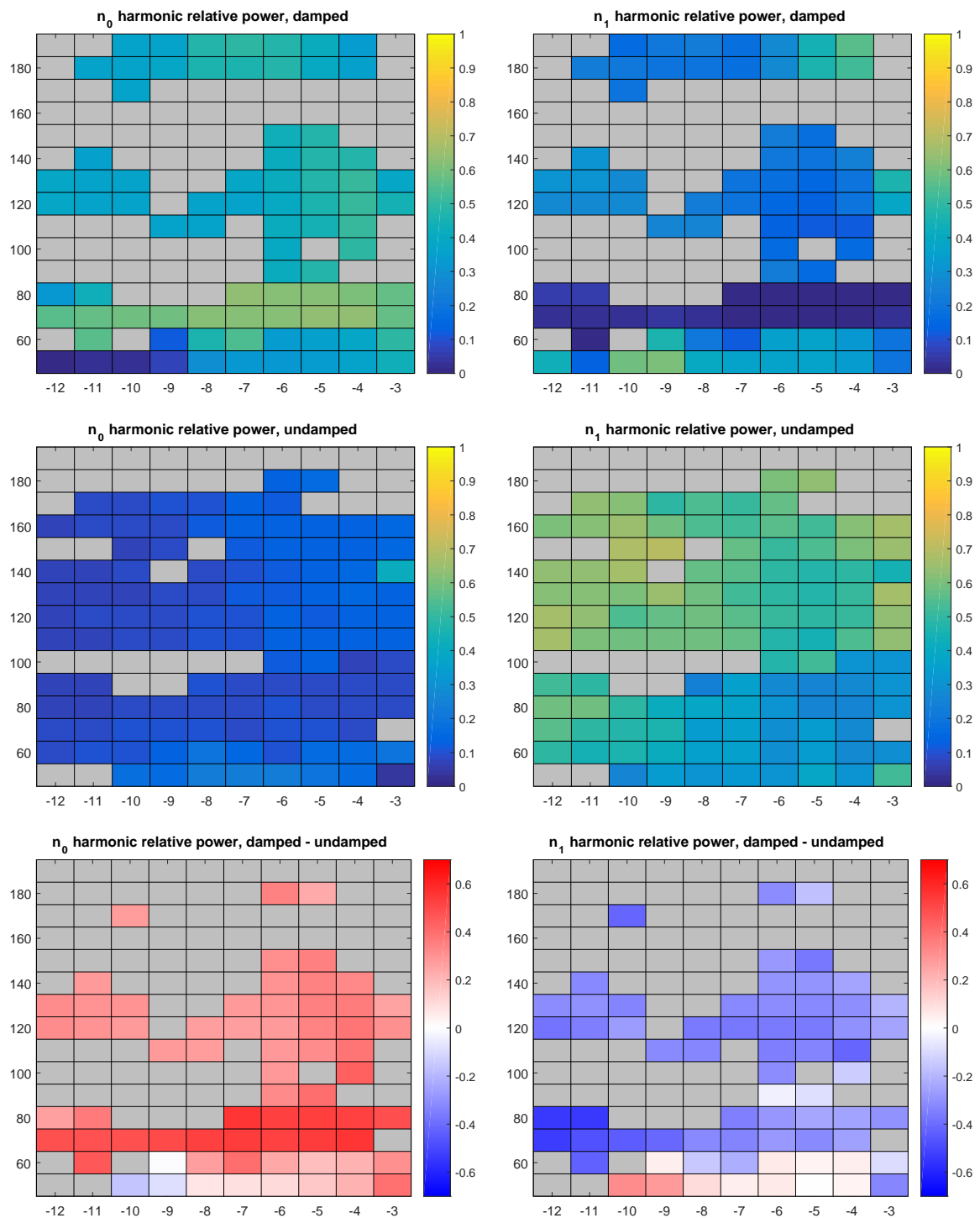


Figure 2.10.: $\beta \approx 1/14$, power of the fundamental and first harmonic frequency, relative to the entire signal. Damped case on top, undamped case in the middle and difference between the two on the bottom. The abscissa defines the bow speed v_b in [cm/s] with negative speeds for up-bow, while the ordinate defines the bow force F_n equivalent mass in [g]. Note the significant difference around an equivalent mass of 80 g.

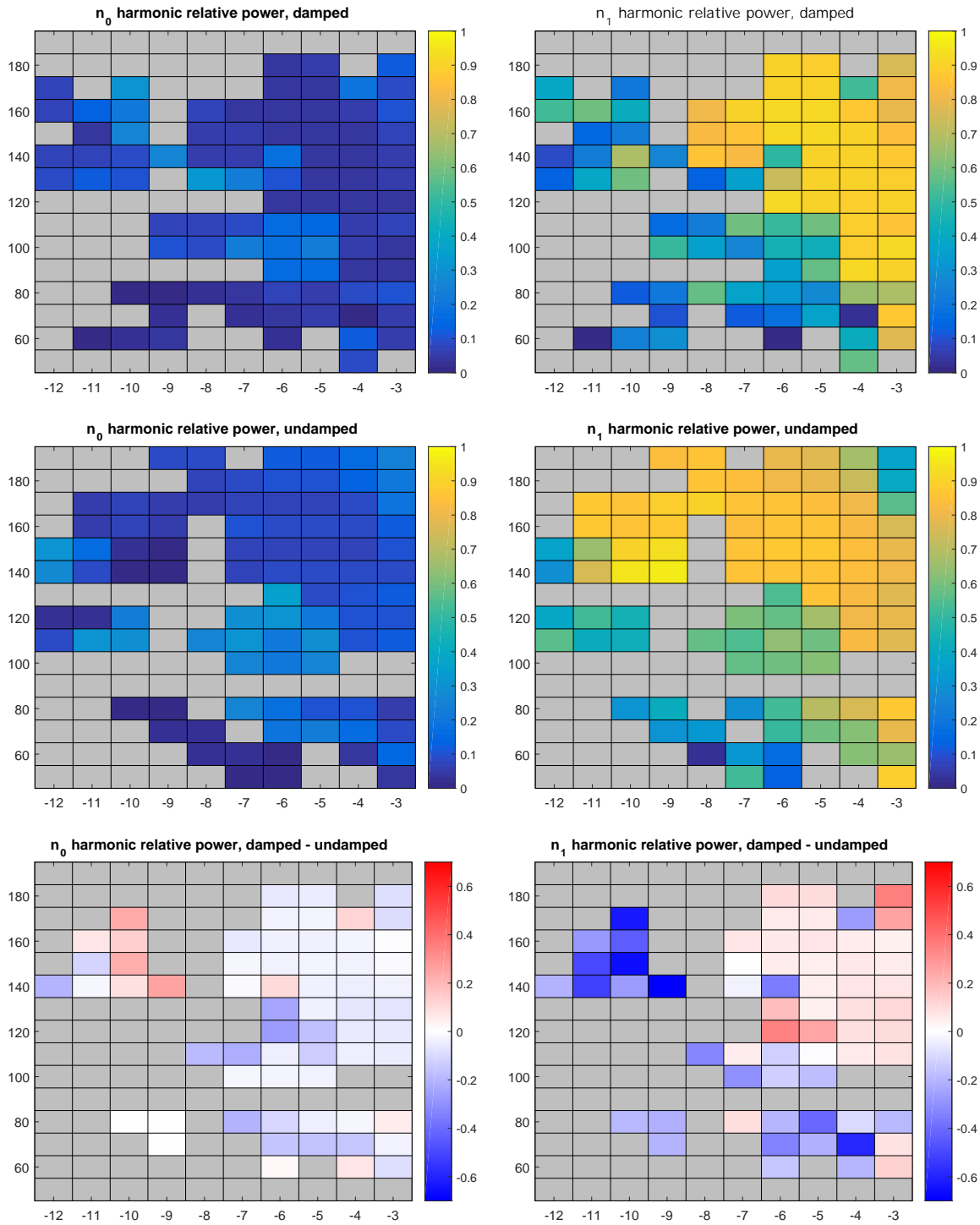


Figure 2.11.: $\beta \approx 1/30$, power of the fundamental and first harmonic frequency, relative to the entire signal. Damped case on top, undamped case in the middle and difference between the two on the bottom. The abscissa defines the bow speed v_b in [cm/s] with negative speeds for up-bow, while the ordinate defines the bow force F_n equivalent mass in [g].

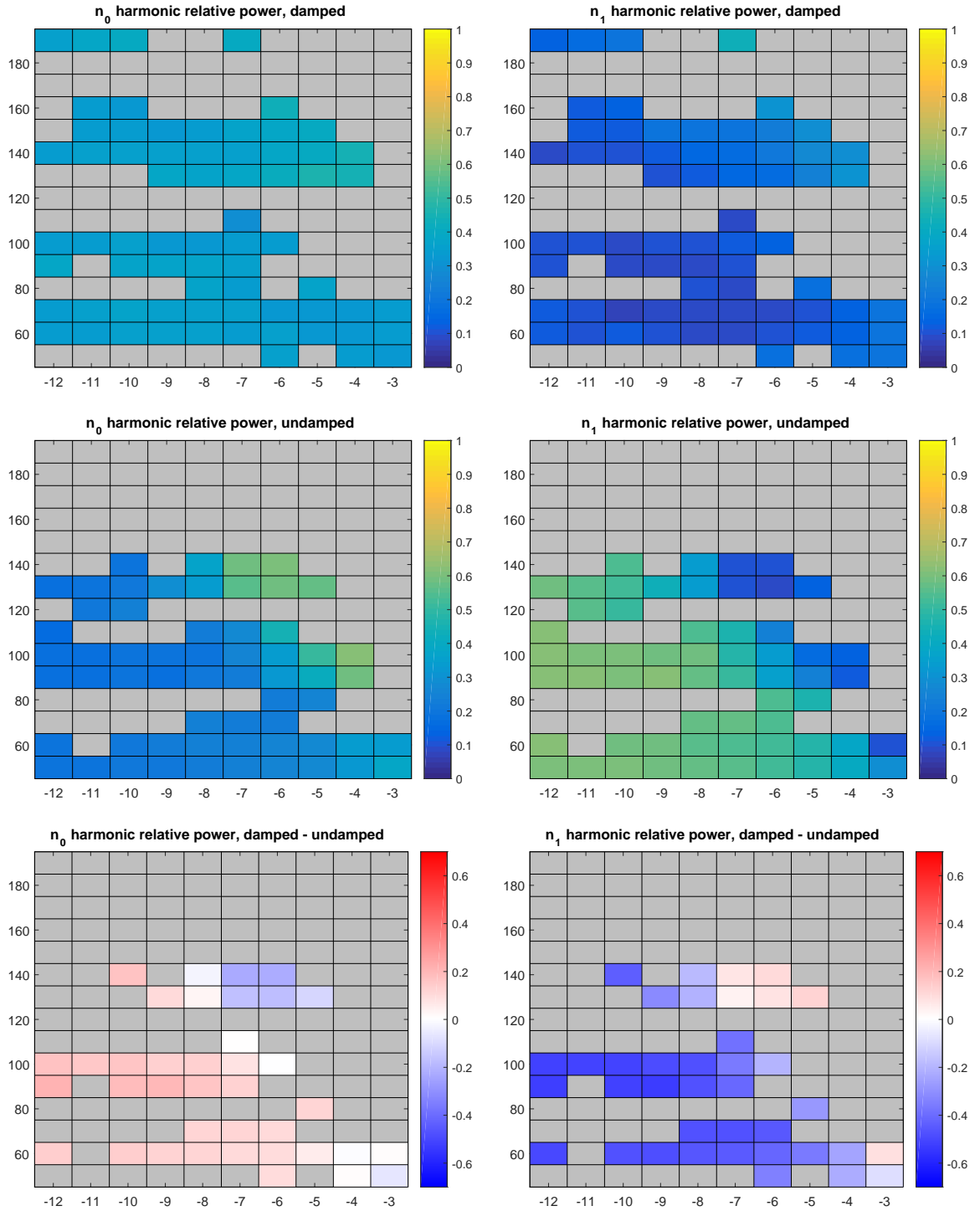


Figure 2.12.: $\beta \approx 1/9$, power content of the fundamental and first harmonic frequency, relative to the entire signal. Free case on top, rigid case in the middle and difference between the two on the bottom. The abscissa defines the bow speed v_b in [cm/s] with negative speeds for up-bow, while the ordinate defines the bow force F_n equivalent mass in [g].

Chapter 3.

Finite Difference Numerical String Simulation

3.1. Physical model ingredients

The following sections describe and summarise the physical string model components and their implementation in a numerical Finite Difference scheme.

A string's transversal and torsional vibrations are well researched, both in theory and experiment [16–19]. Equation (3.1) describes a one-dimensional transversal wave on an ideal, perfectly flexible string placed along the z axis, with string tension T , linear mass density m , transversal string displacement $\eta(z, t)$.

$$T \frac{\partial^2 \eta(z, t)}{\partial z^2} = m \frac{\partial^2 \eta(z, t)}{\partial t^2} \quad (3.1)$$

Transversal wave speed is given by $c_{transversal} = \sqrt{T/m}$ and impedance by $Z_{transversal} = \sqrt{Tm}$. This linearised string equation holds for small amplitude vibrations only, a sufficiently accurate assumption during normal, steady Helmholtz motion of the bowed string. Nevertheless, there are cases of musical interest (e.g. attack transients of the bowed string or forceful plucking), where the vibration amplitude becomes large and a number of nonlinear effects appear, see [20, 21] for an overview.

When fixed at both ends with length L , boundary conditions (3.2) force an analytical and harmonic series of standing wave solutions (3.3), with harmonic number n , amplitude B_n , angular phase shift ϕ_n and $k_n = \frac{n\pi}{L}$.

$$\begin{aligned} \eta(0,t) &= \eta(L,t) = 0 \\ \frac{\partial \eta(0,t)}{\partial t} &= \frac{\partial \eta(L,t)}{\partial t} = 0 \end{aligned} \quad (3.2)$$

$$\begin{aligned} \eta(z,t) &= \sum_{n=1}^{\infty} B_n \sin(\omega_n t + \phi_n) \sin k_n z \\ \omega_n &= k_n v = k_n \sqrt{T/m} \end{aligned} \quad (3.3)$$

These solutions represent the mathematical basis of the harmonic sound produced by stringed instruments. Unfortunately, the non-linear slip and stick interaction between bow hair and string, demands a numerical approach to find solutions. Multiple researchers have implemented finite difference (FD) [22, 23] methods to solve the nonlinear equations of the bowed or struck string. They all added terms to the basic string equation to account for various physical effects.

Ruiz and Hiller [24, 25] first proposed a string model suitable for FD methods, including the bowed string. Later, Bacon and Bowsher [26] focused their research on the struck string.

Chaigne and Askenfelt [27, 28] and later Bensa et al. [29] modelled piano strings struck by a hammer and included damping terms to account for various physical losses and frequency dependent damping of the string.

Pitteroff and Woodhouse [30–32] simulated a model of the bowed string including bending stiffness, torsional motion and longitudinal bow hair compliance. They used FD methods for finite bow hair width simulation, in combination with the analytical solution of the non-interacting string.

Desvages and Bilbao [33] included vertical polarisation of the transversal string displacement without any coupling to the horizontal polarisation and added vertical bow hair compliance. Their model included a term for the bow's inertia instead of a forced bow velocity. Furthermore they modelled the player's left hand fingers, soundboard and string interactions.

This work combines these models as described in Section 3.2, Figures 3.2, 3.3 and Equations (3.10), (3.12) and (3.11). Expanded with a spring and dashpot model of the damping

foam emulating the player's bowing hand, as used during bowing pendulum experiments. Finger and soundboard interactions are neglected, since Chapter 2 includes open string measurements only.

3.1.1. Transversal string displacement

The string is assumed to have tension T , radius a and a homogeneous mass distribution, with linear mass density m . When comparing the more intricate properties of different strings, especially tungsten wound lower cello strings, this may need modification. Following the work of Bensa et al. [29], Equation (3.4) describes the transversal string displacement $\eta = \eta(z, t)$ by adding terms to the ideal, one-dimensional string in Equation (3.1).

$$T \frac{\partial^2 \eta}{\partial z^2} - B \frac{\partial^4 \eta}{\partial z^4} - 2b_1 \frac{\partial \eta}{\partial t} + 2b_2 \frac{\partial \eta}{\partial t} \frac{\partial^2 \eta}{\partial z^2} + f(v_{rel}) = m \frac{\partial^2 \eta}{\partial t^2} \quad (3.4)$$

String bending stiffness $B = \frac{E\pi a^4}{4}$ (Young's Modulus E) adds inharmonicity, where higher modes' frequencies are lowered.

This study uses an external force f modelled after the friction law described in Section 3.1.3.

Chaigne and Askenfelt [27] proposed damping terms to approximate losses occurring in real instruments, due to physical effects such as friction losses or coupling to the instrument's bridge and body. They used first and third order time derivatives to account of frequency dependent damping, where higher frequencies have higher damping factors. Bensa et al. showed that a third order time derivative term leads to an ill-posed initial value problem and instead introduced a mixed spatial and time derivative term b_2 , creating a well-posed initial value problem. They conducted an empirical study with a piano to fit the values of b_1 and b_2 . This work, assuming a crude similarity between the damping behaviour of cellos and pianos, attempts no such study and uses the range empirical values presented by Bensa et al.

Term b_2 , getting larger with increasing frequency, seems to have a stabilising effect on the numerical simulation of Helmholtz motion, as sometimes high frequency perturbations introduced by the non-linear bow hair friction, summed up catastrophically during FD time stepping.

This model of the transversal string displacement is used without modification to introduce a second (perpendicular, uncoupled) polarisation.

3.1.2. String torsion

The bowed string's torsional motion is closely linked to the stick and slip interaction. During sticking, when the relative velocity at a contact point is zero, the string may still roll under the bow hair.

$$v_{rel} = \frac{\partial \eta}{\partial t} - a \frac{\partial \chi}{\partial t} - \frac{\partial x_{hair}}{\partial t} \quad (3.5)$$

Note that when sticking ($v_{rel} = 0$), the string's cross sectional center of mass may still move relative to the bow hair, due to torsional motion.

Formally, torsional motion is described by the same wave equation as transversal motion (3.1). With angular displacement $\chi(z, t)$, torsional stiffness K , moment of inertia per unit length $J = ma^2$, where a is the string's radius and m its linear mass density, assuming a homogeneous mass distribution.

$$K \frac{\partial^2 \chi(z, t)}{\partial z^2} = J \frac{\partial^2 \chi(z, t)}{\partial t^2} \quad (3.6)$$

Torsional wave speed is given by $c_{torsional} = \sqrt{K/J}$ and impedance by $Z_{torsional} = \sqrt{KJ}$.

In principle, modern (cello) strings are usually built with a core wound by a second, different material, which leads to internal friction during torsional motion, thereby dissipating energy, as argued by Woodhouse and Loach [19]. They measured the torsional behaviour of cello strings and their key findings show, that torsional Q factors are roughly an order of magnitude smaller than those of the transverse modes on the same string, while exhibiting only marginal dependence on mode number. The string's material properties used during simulation (Table 3.2) are partially based on their work.

As with the transversal string displacement model, the simulation includes a frequency independent damping term and an external force, dependent on the contact point string velocity relative to the bow hair. In accordance with Woodhouse and Loach's measurements, no frequency dependent damping is included.

$$K \frac{\partial^2 \chi(z,t)}{\partial z^2} - 2d_1 \frac{\partial \chi(z,t)}{\partial t} - af(v_{rel}) = J \frac{\partial^2 \chi(z,t)}{\partial t^2} \quad (3.7)$$

With the dispersion relation $k = \frac{\omega}{c} + i\frac{d_1 c}{K}$, we can relate the damping coefficient d_1 to the torsional Q factor (see Appendix C).

$$Q_0 = \frac{\omega_0 K}{2d_1 c} \quad (3.8)$$

Initial simulations indicate, that the ratio of torsional to transversal Q factors is key to Helmholtz motion stability. Depending on initial conditions, low torsional damping can lead to torsional waves becoming the dominating form of Helmholtz motion. Looking at the identical mathematical form of Equations 3.4 and 3.7, coupled through the external force at the bow hair contact region, it's clear that both wave forms are interchangeable.

3.1.3. Friction model

This work applies the classical velocity dependent friction curve model (Equation 3.9, Figure 3.1), for its success in describing many phenomena of the bowed string. It is based on fitted steady sliding experimental data by Smith and Woodhouse [34]. Multiple researchers have employed it previously (e.g. [33, 35]) and have analysed and discussed it extensively in literature [4] (add Friedlander and more).

$$\mu(v_{rel}) = \pm \left[0.4 \exp \frac{-|v_{rel}|}{0.01} + 0.45 \exp \frac{-|v_{rel}|}{0.1} + 0.35 \right], \quad v_{rel} \leq 0 \quad (3.9a)$$

$$f(v_{rel}) = \mu(v_{rel}) f_b, \quad v_{rel} \neq 0 \text{ (slip)} \quad (3.9b)$$

$$f(v_{rel}) \in [-\mu_s f_b, \mu_s f_b], \quad \mu_s = 1.2 \quad v_{rel} = 0 \text{ (stick)} \quad (3.9c)$$

The tribology of rosin is key to a more sophisticated model of dynamic friction. In particular the rosin's viscosity strongly depends on temperature. Empirical data shows that friction coefficient hysteresis occurs, during dynamic slip and stick processes [34, 36]. This underscores the need for thermal friction models, when looking for a simulation as accurate as possible. Maestre et al. [37] and Mansour et al. [38] have recently implemented thermal friction models in their simulations.

This research should certainly include a thermal friction model in future refinements.

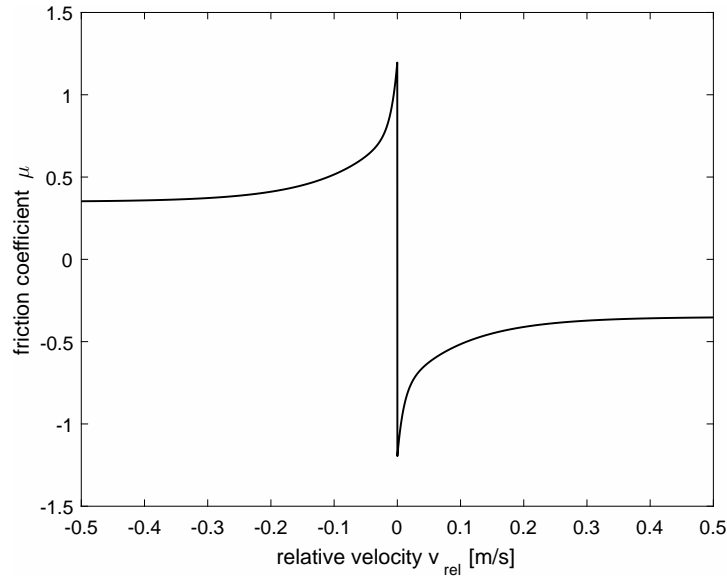


Figure 3.1.: Classical friction coefficient curve (3.9a), after the fit of steady sliding empirical data by Smith and Woodhouse [34].

3.1.4. Bow hair, stick and player's hand

The goal of modelling and simulation in this work, is to identify physical avenues through which the player's bow grip may influence radiated sound. Keeping this in mind, we look at previous research towards understanding the bow hair and stick behaviour.

The bow's history and early scientific work were documented in the nineteenth century by Fétis [39] and Saint-George [40]. Many features of the "modern" bow have been developed by François Xavier Tourte (1750-1835), reaching a sophisticated level of empirical craftsmanship, the physical science's understanding has not caught up to yet, especially with regards to features relevant to musicians and luthiers, such as playability and sound radiation.

Serious scientific interest in the bow, picked up again in the second half of the twentieth century, with papers by Kimball [41] and Reder [42]. In 1975, Schumacher presented experimental and theoretical work on bow hair and sick modes [43].

Guettler and Askenfelt [44–46] Askenfelt measured coupled bow hair and stick modes admittance curves with a tiny accelerometer attached to the bow hair. For longitudinal bow hair vibrations, they found a characteristic impedance of $4\text{--}17 \text{ kg s}^{-1}$, while the steel D string simulated in this work has a characteristic impedance of 0.64 kg s^{-1} . However, they do identify

opportunities for the string to drive the bow, if the bow operates close to a nodal point on the string, where the string impedance is relatively high.

Mansour [35] dismisses any likelihood of bow hair and stick vibrations influencing timbre, due the difference in admittance between string and bow. Although, he acknowledges the bow's importance regarding gestural input and playability.

Recent work by Gough analysed in-plane and out-of-plane vibrational stick modes and their coupling to the bow hair with finite element numerical analysis and comparison with measurements. A key result relevant to this work, Gough found that the player gripping the bow adds significant amounts of damping to the bow hair and stick modes. An entirely plausible fact, since musicians can feel the vibrations of the bow stick and suppress them noticeably with a tight grip. When resting the bow on the string, he did not find any meaningful effects on radiated sound. Although he did remark on the possibility of an effect associated with the detailed slip and stick friction behaviour of the bowed string. Imagine hair and stick vibrating horizontally and vertically in such a manner, that the relative velocity and the force acting on the string, are altered at distinct times during the Helmholtz cycle, thereby facilitating or hindering stick to slip transitions.

The most recent and complete models of the bowed string, still lack definite results on the bow's influence on radiated sound and playability.

This work uses a spring and dashpot model for longitudinal bow hair compliance, as presented by Pitteroff and Woodhouse [30] and implemented by Maestre et al. [37]. Additionally, a lumped model of the bow stick, consisting of a mass coupled to mass of the arm by another spring and dashpot, represents the damping foam/player's hand or possibly a single bow hair and stick vibrational mode. Illustrations are shown in Section 3.2, Figures 3.2 and 3.3.

Based on Desvages and Bilbao's work [33], the vertical bow hair movement is represented by a Hunt-Crossley model [47]. This work neglects any coupling between horizontal and vertical polarisations through the bow hair tension. Since no experimental data to feed the Hunt-Crossley model is available, its values are adjusted "by hand" to give some reasonable vertical bow hair deflection of a few millimetres. During simulation, the resulting bow force F_n is determined by adjusting the vertical position of the arm y_a .

horizontal	
$\boldsymbol{\eta} = \boldsymbol{\eta}(z, t)$	transversal displacement
$\boldsymbol{\chi} = \boldsymbol{\chi}(z, t)$	torsional deflection
$\boldsymbol{x}_h = x_h(z, t)$	bow hair position
$x_b = x_b(t)$	bow stick position
$x_a = x_a(t)$	arm position
vertical	
$\boldsymbol{\zeta} = \boldsymbol{\zeta}(z, t)$	transversal displacement
$y_b = y_b(t)$	bow stick position
$y_a = y_a(t)$	arm position

Table 3.1.: Simulated state variables. The string at rest lies along the z-axis of a cartesian frame of reference, with horizontal transversal displacement along the x-axis and vertical transversal displacement along the y-axis.

3.1.5. Bow driving mechanism

Just as with the bowing pendulum presented in Chapter 2, the mass of the arm is driven by a mass dropping into water. This mechanism has a mechanical impedance of 16.6 kg s^{-1} , as shown by experimental data by Mores [2]. The bow speed is adjusted by changing the mass dropping into water.

3.2. Model summary

The bowed string model presented in Figures 3.2, 3.3 and Equations (3.10) to (3.12), is suitable for finite difference numerical simulation, with explicit time stepping. State variables are defined in Table 3.1. As laid out in the previous sections, the model includes bending stiffness, linear damping, dispersion, uncoupled horizontal and vertical transversal polarisation, string torsion, finite bow width, longitudinal bow hair compliance, a lumped model of the player's hand and arm and the classical velocity dependent friction coefficient. There is no forced bow velocity, instead the system self adjusts to the impedance w , modelled after a mass dropping into water driving the bow. Model and string parameter magnitudes are given in Table 3.2, corresponding to a cello D string (tuned to 147 Hz) and taken from various sources in literature as indicated.

Horizontal model equations.

$$T\eta'' - B\eta'''' - 2b_1\dot{\eta} + 2b_2\eta''\dot{\eta} + f(v_{rel}) = m\ddot{\eta} \quad \text{transverse} \quad (3.10a)$$

$$K\chi'' - 2d_1\dot{\chi} - af(v_{rel}) = J\ddot{\chi} \quad \text{torsion} \quad (3.10b)$$

$$k_h(x_b - \mathbf{x}_h) + c_h(\dot{x}_b - \dot{\mathbf{x}}_h) + f(v_{rel}) = m_h\ddot{\mathbf{x}}_h \quad \text{bow hair} \quad (3.10c)$$

$$-k(x_b - x_a) - c(\dot{x}_b - \dot{x}_a) + k_h(\mathbf{x}_h - x_b) + c_h(\dot{\mathbf{x}}_h - \dot{x}_b) = m_b\ddot{x}_b \quad \text{bow stick} \quad (3.10d)$$

$$k(x_b - x_a) + c(\dot{x}_b - \dot{x}_a) + m_g g - w\dot{x}_a = m_a\ddot{x}_a \quad \text{arm} \quad (3.10e)$$

$$\dot{\eta} - a\dot{\chi} - \dot{\mathbf{x}}_h = v_{rel} \quad (3.10f)$$

Vertical model equations.

$$T\zeta'' - B\zeta'''' - 2b_1\dot{\zeta} + 2b_2\zeta''\dot{\zeta} - f_b(\Delta\mathbf{y}_h) = m\ddot{\zeta} \quad \text{transverse} \quad (3.11a)$$

$$k(y_a - y_b) + c(\dot{y}_a - \dot{y}_b) - m_b g + f_b(\Delta\mathbf{y}_h) = m_b\ddot{y}_b \quad \text{bow stick} \quad (3.11b)$$

$$y_b - \zeta_{contact} + a = \Delta\mathbf{y}_h \quad \text{bow hair} \quad (3.11c)$$

$$y_a = \text{const.} \quad \text{arm} \quad (3.11d)$$

Clamped boundary conditions.

$$\eta(0,t) = \eta(L,t) = 0 \quad (3.12a)$$

$$\dot{\eta}(0,t) = \dot{\eta}(L,t) = 0 \quad (3.12b)$$

$$\chi(0,t) = \chi(L,t) = 0 \quad (3.12c)$$

$$\dot{\chi}(0,t) = \dot{\chi}(L,t) = 0 \quad (3.12d)$$

$$\zeta(0,t) = \zeta(L,t) = 0 \quad (3.12e)$$

$$\dot{\zeta}(0,t) = \dot{\zeta}(L,t) = 0 \quad (3.12f)$$

Note, that the horizontal transversal displacement and torsional deflection are coupled through the friction force $f(v_{rel})$. When sticking, the string rolls under the bow hair, balancing the torsional and transversal restoring forces with the friction forces.

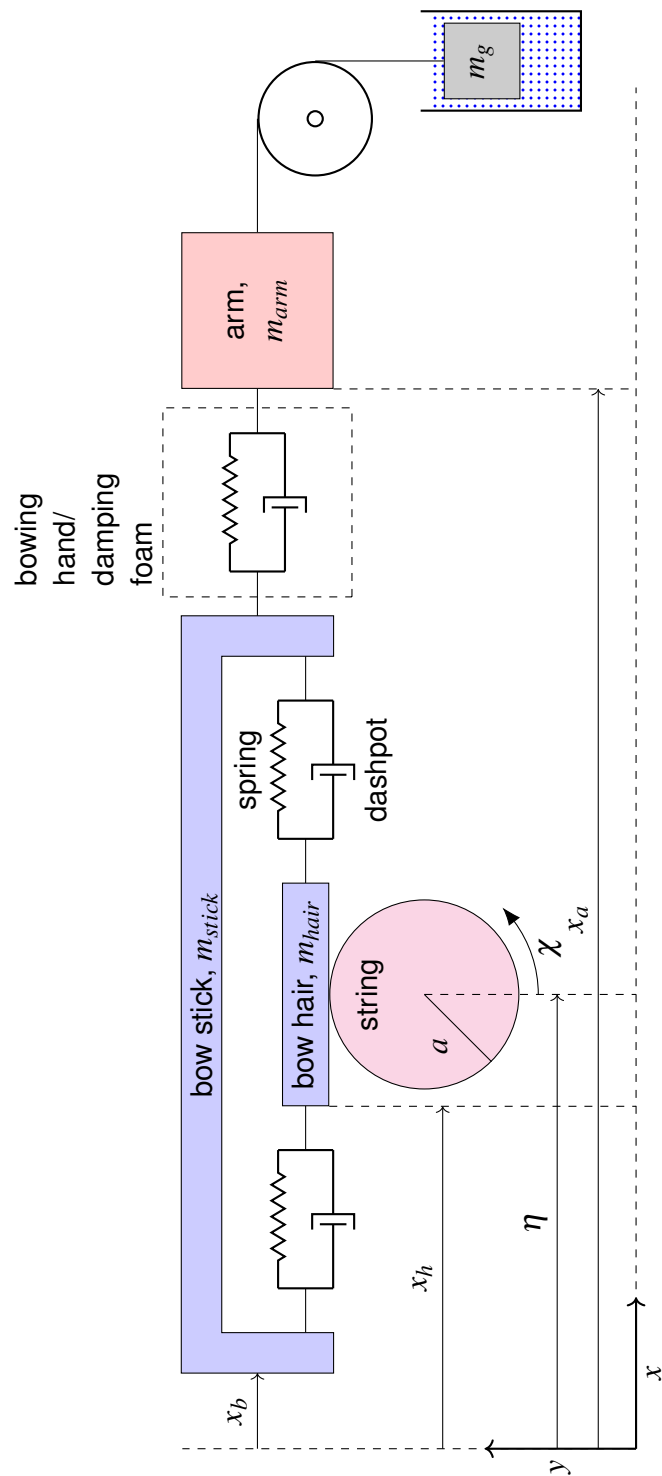


Figure 3.2.: Horizontal polarisation bowing model.

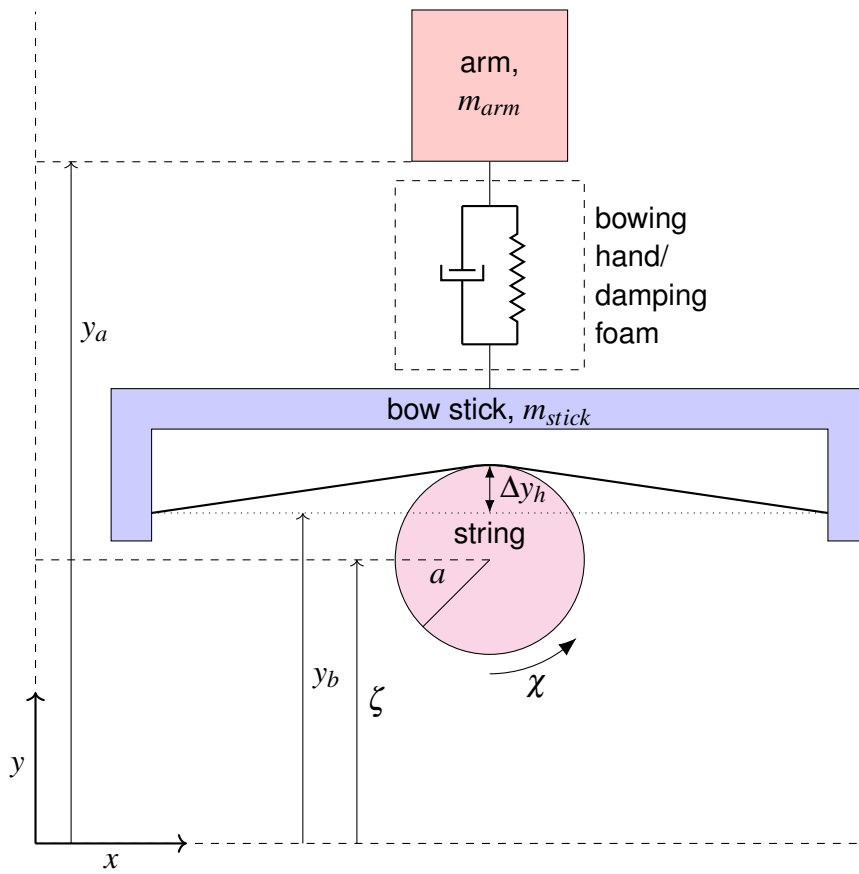


Figure 3.3.: Vertical polarisation bowing model.

L	string length	0.685	m
T	string tension	130	N
$B = \frac{E\pi a^4}{4}$	bending stiffness	3×10^{-4}	Nm^2
m	linear mass density	0.0032	kg m^{-1}
b_1	transversal damping coefficient	0.0019	$\text{kg s}^{-1} \text{m}^{-1}$
b_2	transversal damping coefficient	4.8×10^{-7}	kg m s^{-1}
$K = \frac{G\pi a^4}{4}$	torsional stiffness [19]	2.8×10^{-4}	Nm^2
$J = \mu a^2$	moment of inertia per unit length [19]	6.9×10^{-10}	kg m
a	string radius	0.465×10^{-3}	m
d_1	torsional damping coefficient [19]	2.5×10^{-8}	kg m s^{-1}
k	foam spring constant	500	Nm^{-1}
c	foam damping coefficient	9.9	kg s^{-1}
k_h	dist. bow hair spring constant [30]	6×10^6	Nm^{-2}
c_h	dist. bow hair damping coefficient [30]	1×10^3	$\text{kg s}^{-1} \text{m}^{-1}$
m_b	bow stick mass	0.08	kg
m_a	arm mass	3	kg
m_g	driving mass	variable	
w	driving unit impedance	16.6	kg s^{-1}

Table 3.2.: Cello D string model parameters. E : Young's Modulus, G : Shear Modulus.

3.3. Time-stepping algorithm

The Finite Difference method implementation is detailed in Appendix B. The resulting basic time-stepping equations are given by

$$\mathbf{s}^{j+1} = \mathbf{A}^j \mathbf{s}^j + \mathbf{A}^{j-1} \mathbf{s}^{j-1} + \mathbf{A}^{j-2} \mathbf{s}^{j-2} + (\mathbf{M}^{j+1})^{-1} \mathbf{f}, \quad (3.13)$$

where vector \mathbf{s}^j at time step j contains all state variables and the square FD matrices \mathbf{A}^j , \mathbf{A}^{j-1} , \mathbf{A}^{j-2} and $(\mathbf{M}^{j+1})^{-1}$ contain all model parameters.

Numerically, the relative velocity between bow hair and string is never exactly zero. Figure 3.4 depicts an offset added to the friction curve, taking this problem into account.

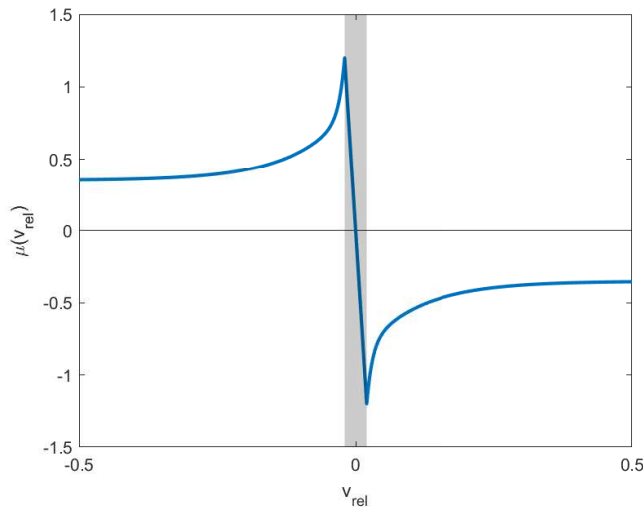


Figure 3.4.: Classical friction coefficient curve, with a numerical offset. The shaded area indicates sticking.

Using this friction curve with a numerical offset with the slip FD equations (B.13) — assuming $v_{rel} < \text{offset}$ means sticking — involves a trade-off between the maximum stick relative velocity (small offset preferred) and the algorithm's propensity to oscillate between sticking and slipping in alternating time steps (large offset preferred). If the offset is too large, small effects such as Schelleng ripples may be obscured and if it is too small, the bow may fail to stick entirely during simulation.

To avoid this conundrum, a sufficiently small offset ($1 \times 10^{-6} \text{ m s}^{-1}$) is used and during sticking, the relative velocity is forced to zero (within numerical accuracy) by using the stick FD

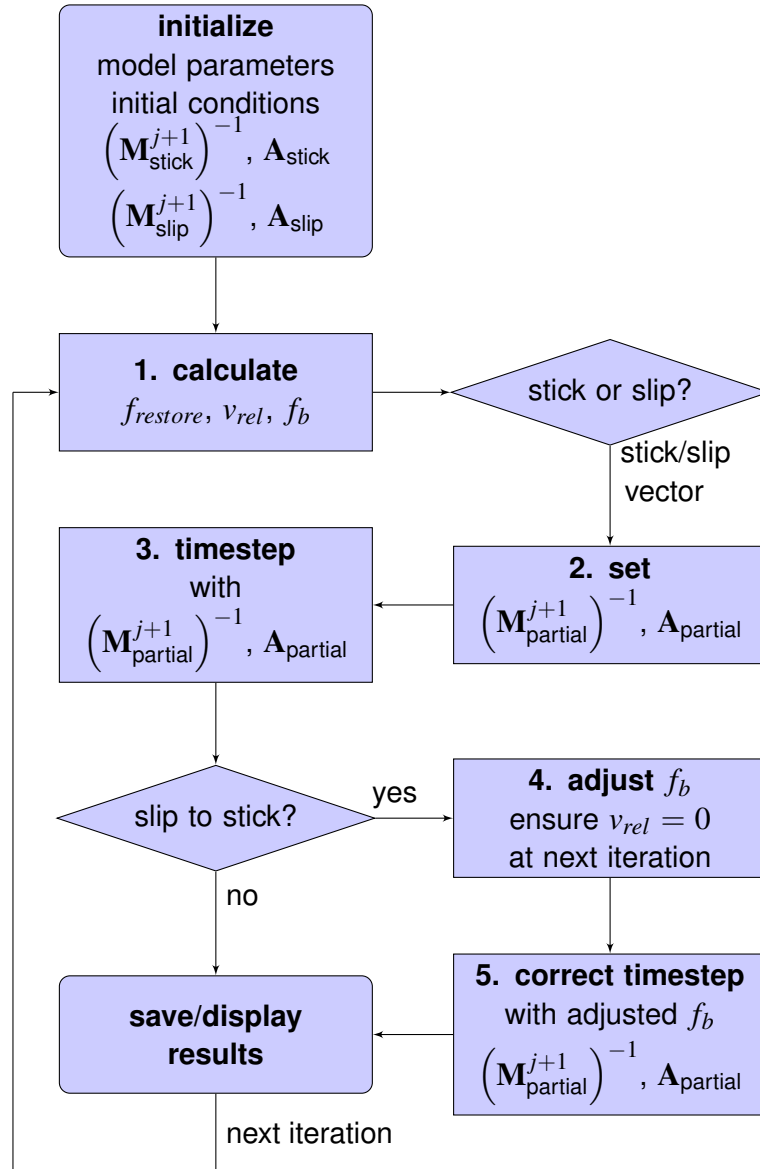


Figure 3.5.: Time-stepping algorithm workflow when using separate FD equations for (partial) sticking or slipping situations.

equations (B.15). Now, during sticking the friction force assumes the value of the string's restoring forces (B.14), ensuring $v_{rel} = 0$.

As presented in Figure 3.5, after initialization, the time-stepping loop starts by

1. taking the string's restoring forces from the previous time-step and calculating the relative velocity and bow force using backwards FD equations (B.10). If $|v_{rel}| < \text{offset}$ and $|f_{restore}| < f_b$, the bow hair sticks to the string.
2. Set the correct FD matrices according to the slipping or sticking state of each bow hair and string contact grid point.
3. Perform timestep according to Equation (3.13) and check whether grid points changed from slipping to sticking. (When $|v_{rel}| < \text{offset}$ or changes its sign and $|f_{restore}| < f_b$.)
4. When a slipping grid point changed the sign of its relative velocity during, it should start sticking. To ensure this, an iterative numerical solver (*Dogleg* algorithm [48]), solves Equation (3.13) for f_b with the constraint $v_{rel} = 0$.
5. The timestep is repeated with the (slightly) adjusted f_b .

Setting the partial slip and stick FD matrices and running the numerical solver is computationally expensive. On the other hand, this time-stepping algorithm produces numerically much more reliable transitions between slipping and sticking.

3.4. Simulation results

3.4.1. Average power and spectral centroid analysis

Consistent with the bowing pendulum experiments in Chapter 2, the simulation results presented in Figure 3.6, are restricted to steady Helmholtz motion, with a congruent parameter space exploration and, again, with the simple metrics of spectral centroid and power in the 20 - 10000 Hz band. They are calculated from the string's transverse displacement 1 mm away from the bridge, since the instrument body is not simulated. The calculation methodology is identical (Section 2.2), with a short-time fourier transform (16384 samples window length at 50 kHz sample rate) and a YIN algorithm [12] for Helmholtz motion classification purposes.

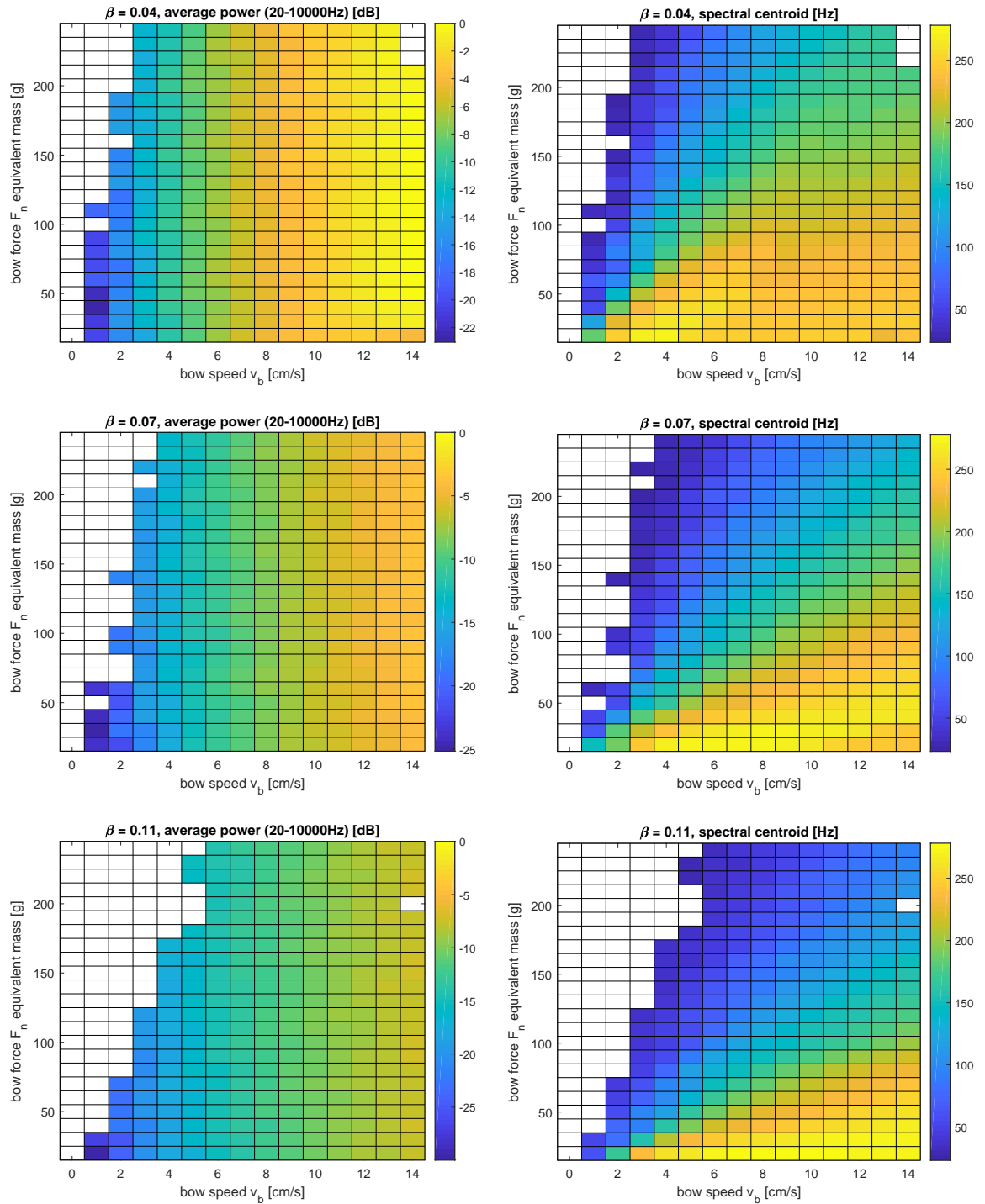


Figure 3.6.: Pseudocolour plots of the average power in the 20 - 10 000 Hz frequency range and spectral centroid across the playing parameter space spanned by F_n and v_b , at three distinct values of β . Calculated from the string's transverse displacement 1 mm away from the bridge. Each coloured rectangle represents an average over multiple *stft* windows. Power in dB is given relative to the rectangle with the highest output.

A direct comparison with the microphone signal presented in Sections 2.3.2 and 2.3.3 is obviously questionable, nevertheless a few basic observations seem allowable. The model properties used, do not result in any relevant bow stick vibrations, while longitudinal bow hair vibrations do occur.

The average power output increases with bowing velocity, but remains entirely independent of F_n . When approaching the bridge, power output increases. At medium and large β , this behaviour is consistent with the empirical findings for the rigid bow mounting in Figure 2.9.

The spectral centroid pseudocolour plots (Figure 3.6, right column) display close to linear trajectories of constant centroid in the $v_b - F_n$ plane. A general trend of lower spectral centroid at low v_b and high F_n , and higher spectral centroid at high v_b and low F_n is observable. At constant values of v_b and F_n , the spectral centroid increases when bowing closer to the bridge. At low v_b and low F_n , the $\beta = 0.04$ plot (top right) exhibits a maximum in spectral centroid, shifting to higher bow speed, when moving away from the bridge. Overall and in absolute terms no bowing position β can lead to a distinctly higher spectral centroid. There are no clear parallels to be extracted, when comparing the spectral centroid simulation and empirical results.

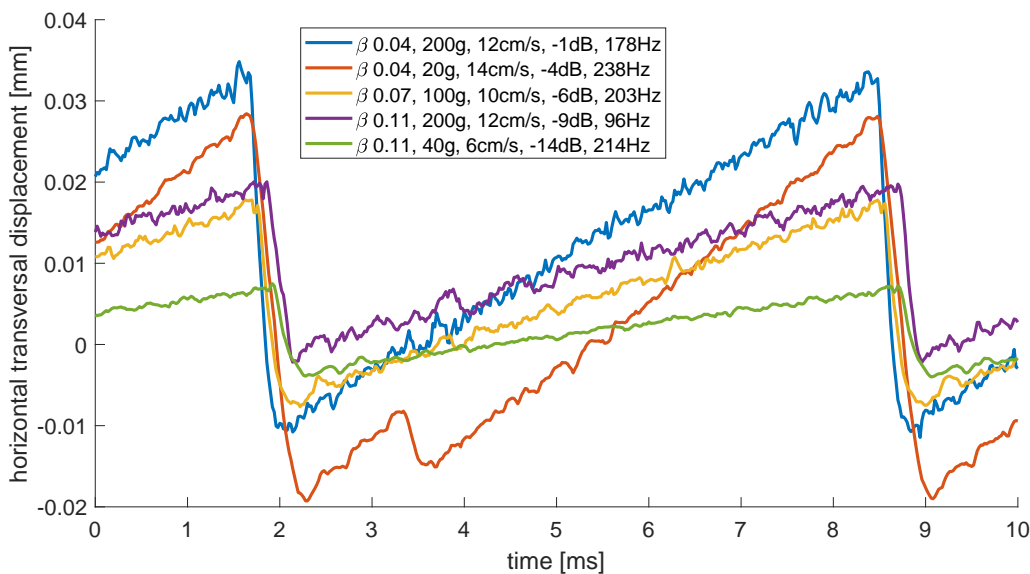


Figure 3.7.: Select examples of horizontal transverse displacement, 1 mm away from the bridge, single slip and stick cycle. The legend indicates β , bow force equivalent weight, bow speed, average power and spectral centroid. The average power and spectral centroid analysis in Figure 3.6 is based, in part, on this data.

Figure 3.7 shows select examples of the horizontal transverse displacement, 1 mm away from the bridge, used for average power and spectral centroid calculation. The examples, showing a single cycle of Helmholtz motion each, are synced at the moment of string release. The correlation between amplitude and average power is immediately apparent to the naked eye, while the particular value of spectral centroid is not related to the displacement curve shape in an obvious manner. The next section investigates the precise slip and stick interaction between bow hair and string with the chosen examples.

3.4.2. Partial slip, string torsion and bow hair vibrations

The strength of the simulation model at hand, is its inclusion of the finite width contact area, torsional string motion and longitudinal bow hair vibrations. The three model components are tightly linked and related to the concept of *Schelleng Ripples*.

The previous section's examples are investigated in Figures 3.8 to 3.12, where the top plot presents horizontal transverse displacement and torsional deflection (at the contact area's center) in relation to the moment of string release, where all bow hair segments start slipping, as indicated by the vertical black lines. The middle graph depicts relative velocity between string surface and bow hair v_{rel} and the velocity difference between the string's cross sectional center and the bowing velocity v_b , corresponding to the relative velocity measured in much of the empirical literature available. The bottom graph presents the slip and stick interaction across the entire contact area width. White corresponds to sticking (remember, the string may still roll), red indicates slipping backwards with respect to the bowing direction and blue represents forward slipping. Note that axis scaling is kept constant across all figures.

Example 1 (Figure 3.8) corresponds to playing *piano*, at low v_b and F_n , close to the fingerboard, while example 2 (Figure 3.9) corresponds to playing *forte*, at high v_b and F_n , close to the bridge. Both playing states present close to ideal Helmholtz motion, with relatively few partial slips and sharp slip to stick transitions. The *piano* example has almost no ripples during the sticking phase, as seen both in relative velocity and transverse displacement. The *forte* case exhibits slightly stronger ripples, associated with partial slips that reach further across the bow hair width — but almost no forward slips — and a higher torsional deflection, both in amplitude and absolute offset. The highly irregular relative velocity $v_{center} - v_b$ is a result of longitudinal bow hair vibrations. Closer to the bridge, the time spent slipping is shortened and maximum slip velocity is reached only momentarily, although it is about four

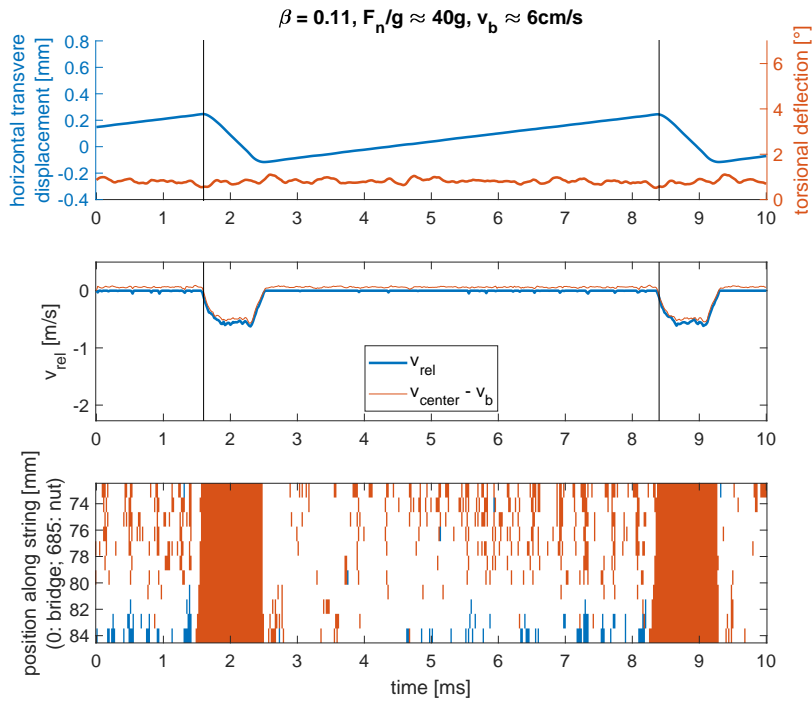


Figure 3.8.: example 1, *piano*. Average power -14 dB, spectral centroid 214 Hz.

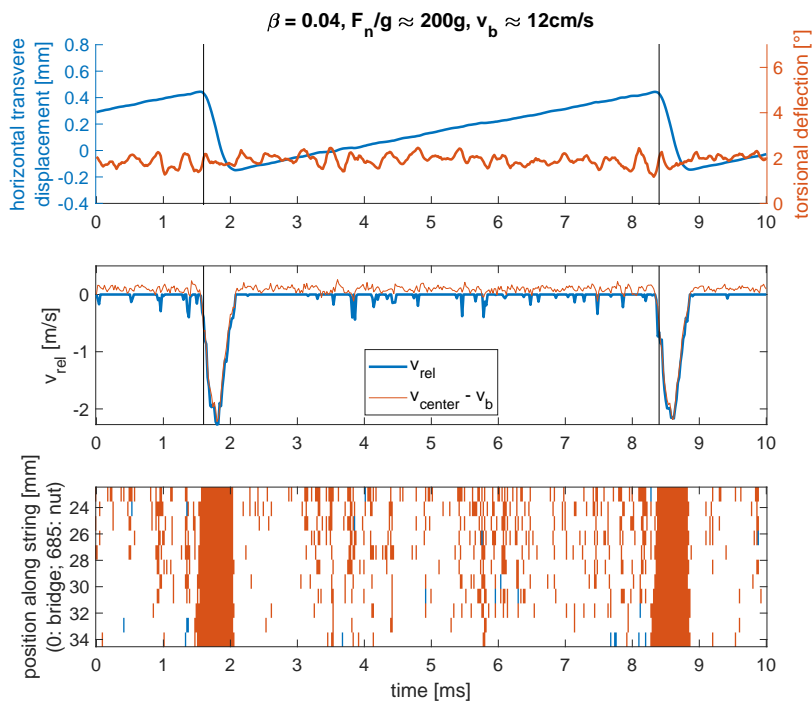


Figure 3.9.: example 2, *forte*. Average power -1 dB, spectral centroid 178 Hz.

times higher than in the *piano* case. When looking closely, the moment of slip initiation and the torsional vibration follow a fixed phase relationship. With *piano*, release occurs close to the minimum torsional deflection and with *forte*, release occurs during forward rotation (in bowing direction).

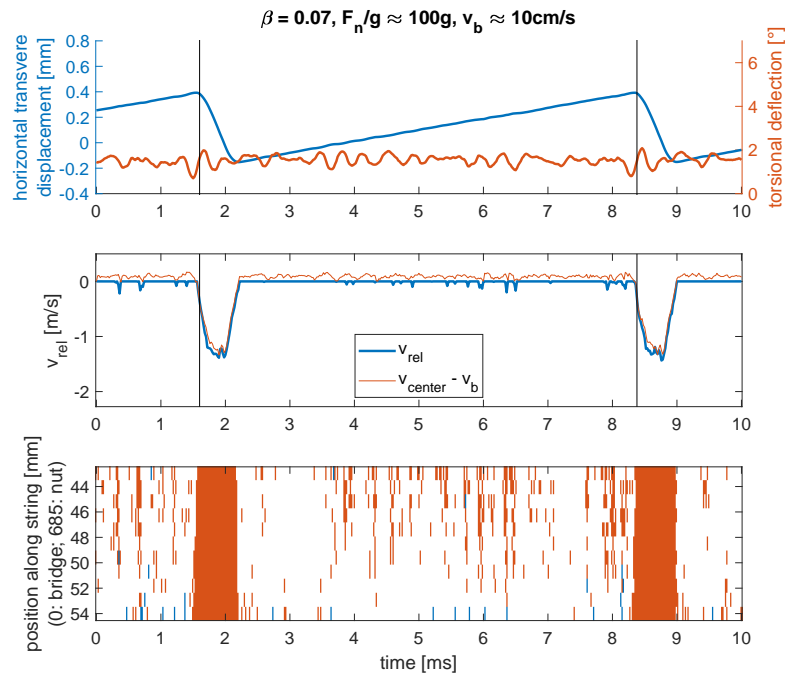


Figure 3.10.: example 3, medium β , close to ideal Helmholtz motion. Average power -6 dB, spectral centroid 203 Hz.

Example 3 (Figure 3.10) depicts close to ideal Helmholtz motion at intermediate playing parameters. A correlation between the relative velocity $v_{center} - v_b$ ripples and torsional deflection is apparent. Again, supporting the notion that the ripples during the stick phase are formed through a combination of torsional vibrations, longitudinal hair vibrations and partial slipping. Furthermore, the fixed phase relationship between release and torsional deflection is present (release during forward rotation).

Example 4 (Figure 3.11), although there are multiple release events during the Helmholtz cycle, is still classified as Helmholtz motion by the fundamental frequency estimating YIN algorithm. The main slip event and Helmholtz corner are clearly visible. The second release manifests itself as a strong ripple, illustrating a rather fluid transition from Helmholtz motion to non-Helmholtz motion when approaching the minimum bow force. Torsional deflection amplitude and offset are at a minimum. The majority of the time, much of the contact area is

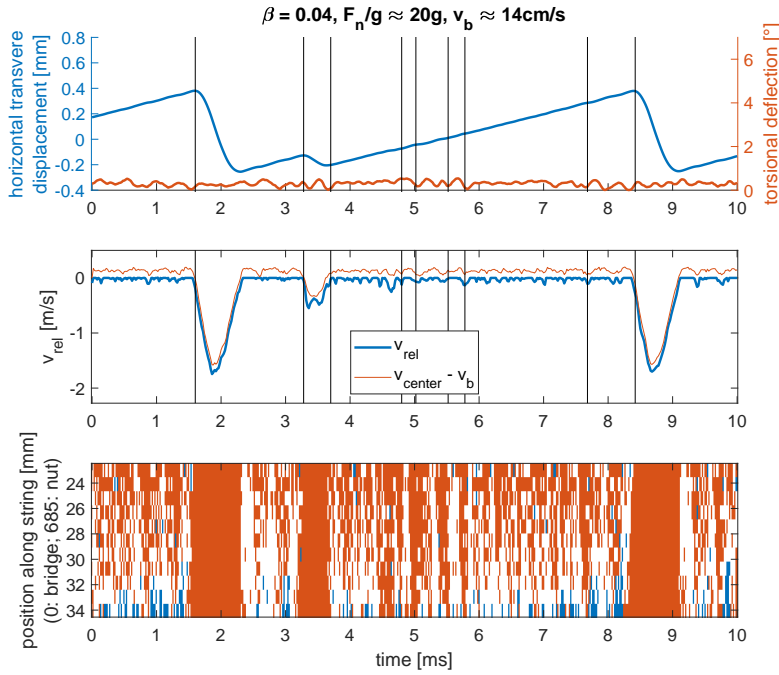


Figure 3.11.: example 4, multiple slipping. Average power -4 dB, spectral centroid 238 Hz.

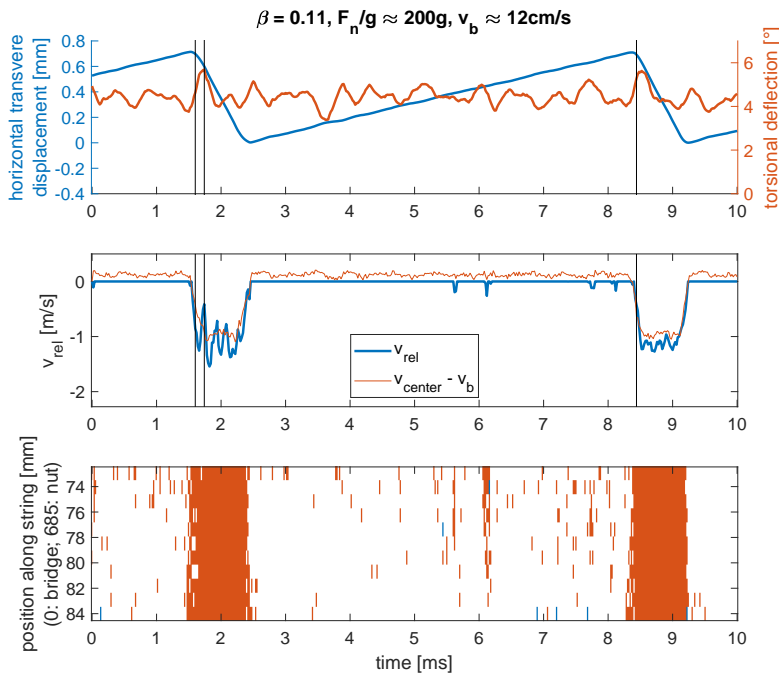


Figure 3.12.: example 5, strong torsional vibration. Average power -9 dB, spectral centroid 96 Hz.

slipping, nevertheless the slip and stick characteristic continues to emerge. Again, the main release occurs during forward rotation.

Example 5 (Figure 3.12) is a sort of brute force example close to the fingerboard. During musical play this would be rather an exception than the norm. Almost no partial slips occur, but quite noticeable, the stick to slip transition is not instantaneous, as some bow hair segments slip and stick repeatedly. As a result the v_{rel} curve shows stronger vibrations during slipping. As with the previous examples, release occurs during forward rotation. Remarkably, despite the high torsional amplitude and offset, barely any ripples occur during the sticking phase.

3.5. Summary of findings

The numerical simulation model presented in this work, succeeds at modelling steady Helmholtz motion, with two uncoupled transverse directions of polarisation, torsional motion, dispersion, frequency dependent damping, longitudinal bow hair compliance, finite bow hair width and a low mechanical impedance driving mechanism modelled after Mores' bowing pendulum. The classical velocity dependent friction curve was implemented. An offset in the friction curve is kept to a minimum by using a separate set of model equations during slipping and sticking.

A non-exhaustive β , v_b and F_n parameter space analysis of steady Helmholtz motion was conducted. Average power and spectral centroid behaviour, calculated with a short-time fourier transform, was investigated. The parameter dependence of the average power shows good agreement with empirical evidence, while, unsurprisingly, modelling the spectral centroid behaviour correctly may require sophisticated analysis and modelling of bridge, body and bow stick-hair resonances with coupled transverse polarisations.

No clearly visible relationship between the rounding of the Helmholtz corner and spectral centroid can be extracted from the transverse displacement data.

An analysis of finite bow hair width slip and stick behaviour proved to be fruitful. The effects of partial slipping (forward and backward), torsional motion and longitudinal bow hair vibrations all influence the ripples — visible in both the transverse displacement and relative velocity curves — during the sticking phase of the Helmholtz cycle, to a varying degree, dependent on the bowing parameter. No clear dominating effect emerged.

3.5. Summary of findings

Release events and torsional motion follow a strict phase relation. Release always occurred near the minimum torsional deflection or later during forward (in bowing direction) rolling.

The Helmholtz motion seems exceptionally resilient to partial slipping, even when more slipping than sticking, across the entire bow hair width, occurs, continuous Helmholtz motion can persist.

These results emphasize, that finite bow hair width simulation is essential to understanding the detailed nature of the slip and stick friction interaction and working towards improved friction models.

Chapter 4.

Conclusions and Outlook

Grappling with the understanding of the bowed string and its playability, is possible on different levels of analysis. An empirical, measurement techniques based approach, was presented in Chapter 2. Physics based modelling, trying to describe and understand the bowed Instrument's nature at a fundamental level, was elaborated on in Chapter 3. At the same time, a musical perspective, thinking like a musician, luthier, bow maker or listener, seems to be of equal importance, as their level of sophistication stems from long tradition and their craft was honed over centuries.

When entering the domain of musicians, we invariably travel to the realm of aesthetics, subjective perception and emotion, posing an additional, uncertain challenge. And yet we can certainly strive to classify what constitutes playability and great sound, further refining our models to include the bow, instrument body and musician's physiology in greater detail.

The bowing pendulum experiments presented in this work, provide empirical evidence of the bowing hand's influence on the frequency spectrum and radiated sound level, beyond the three major bowing parameters (F_n , v_b , β). To provide further insight and relate these results to musical playing and listening traditions, further auditory perception studies and measurements of musician's muscle tension are required.

The results in Chapter 2 support the use of a bowing pendulum, rather than electrically driven bowing machines. Nevertheless, the present bowing pendulum has room for improvement. A more elaborate bow mounting, akin to a musician's bow grip and with tuneable damping properties is desirable. As is some form of automated measurement. With the current setup, adjusting the bow forces and fine tuning the pendulum is a quite tedious task.

The empirical data on the bowed string currently available, is insufficient to accurately verify the presented model of the bowed string. Horizontal and vertical string displacement, torsional and thermal data, across the finite bow hair width, with sufficient time resolution are necessary. Further bowing pendulum experiments should incorporate advanced sensors to simultaneously measure and derive more string model parameters with greater precision, in order to work towards practical applications useful to luthiers, string manufacturers or musicians.

The physics based model established in this work, is successful in describing the torsional motion of the string and the associated partial slipping and forward slipping phenomena. Incorporating a thermal friction model is key and necessary improvement in further work. The finite difference model at hand could be used, to further investigate the bowed string's torsional motion. The processes facilitating a fixed phase relation between torsional motion and release, are poorly understood. Inácio [49] has shown, that the ratio of transversal to torsional wave speed, can influence the duration of transitions. This could be investigated further, presenting an avenue to understand playability.

Unfortunately, the finite difference modelling efforts have reached somewhat of a dead end, particularly in terms of performance, especially when attempting elaborate parameter space analysis. Further model refinements, should ideally include a modal analysis of the instrument's body and bridge as well as the bow's hair and stick. Coupling between transverse polarisations is key when trying to analyse the influence of bow stick vibrations. It is conceivable, that a (tiny) Helmholtz like motion occurs in vertical direction of transverse polarisation. Leading to bow force and velocity variations, supporting or hindering particular qualities of the bowed string. Combined digital waveguide synthesis and finite difference methods show more promise to achieve high fidelity and real-time performance.

When listening, the emerging patterns of music, provide us with deep satisfaction, a maybe primordial experience at times. A great understanding of nature's processes and the sophistication of precise measurement, are rewarding in themselves. Reasons, other than personal and cultural, to further pursue this avenue of research, do exist. Some Luthiers like to enhance their craftsmanship with the tools of modern physics, to more reliably achieve a high level of perfection. Certainly, measurement techniques can bring some objectivity to the otherwise quite subjective listening experience, when judging combinations of instrument, string and bow. Musicians with their very much individual preferences, are often left with the (sometimes expensive) process of trial and error, when choosing the right combination. Some level of predictability from measured data, to identify desired combinations of good tonal quality

and playability would be useful indeed. There are tradeoffs involved between playability and different aspects of tonal quality. This is also the case when manufacturing strings. Making predictions based on a set of string parameters and material properties, would provide string manufacturers with an advantage. In future, it might even be conceivable, to develop a virtual instrument closely resembling reality, allowing musicians to easily test and compare the sound of multiple different strings.

Appendix A.

Scatter plots

A.1. Spectral centroid

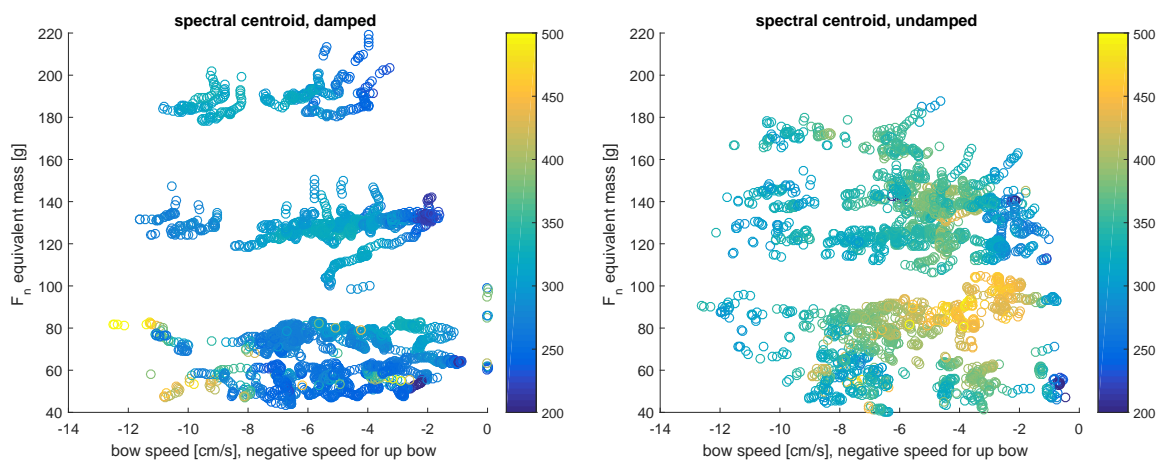


Figure A.1.: $\beta \approx 1/14$, spectral centroid scatter plot.

Appendix A. Scatter plots

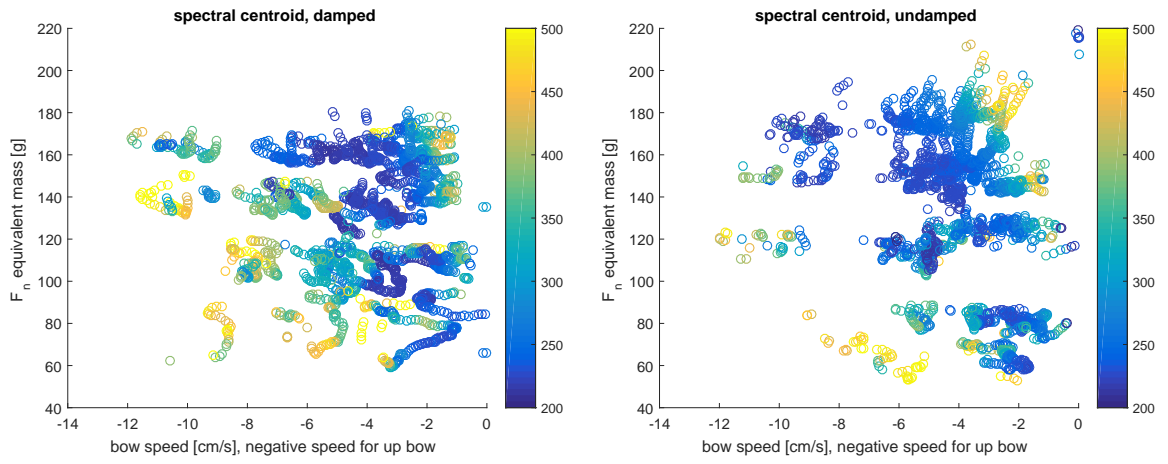


Figure A.2.: $\beta \approx 1/30$, spectral centroid scatter plot.

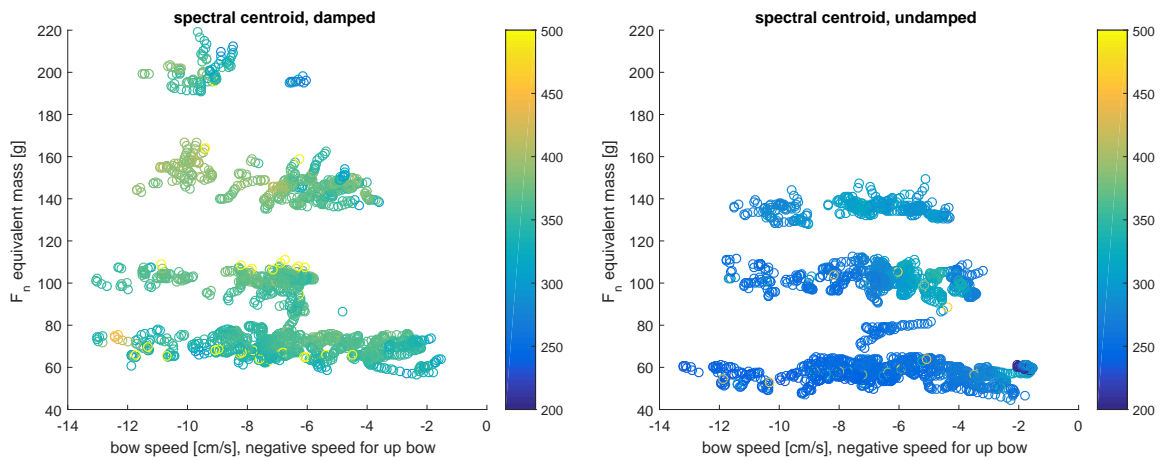


Figure A.3.: $\beta \approx 1/9$, spectral centroid scatter plot.

Appendix B.

Finite Difference Method Implementation

B.1. Equally Spaced Discretisation Grid

Finite Difference Simulations were performed on an equally spaced discretisation grid with an explicit time-stepping method. Separate grid points were used for horizontal transversal, vertical transversal and torsional motion. The number of grid points is calculated from the string length L and grid spacing Δz .

$$N = \frac{L}{\Delta z} \quad (\text{B.1})$$

Discrete horizontal transversal displacement vector notation at time step j .

$$\eta(z, t) = \begin{pmatrix} \eta_1^j \\ \vdots \\ \eta_N^j \end{pmatrix}, \text{ with } \eta_i^j = \eta(z_i, t_j) \quad (\text{B.2})$$

Throughout this chapter, index i denotes grid points along the entire string, while index c denotes the $W = e_2 - e_1$ grid points within the string and bow hair contact region, where e_1 and e_2 index the bow hair edge grid points.

$$i \in [1, \dots, N] \quad (\text{B.3a})$$

$$c \in [e_1, \dots, e_2], \text{ with } e_1, e_2 \in [1, \dots, N] \quad (\text{B.3b})$$

We can summarise all $3N + W + 4$ simulated state variables in a single discrete vector.

$$\mathbf{s}^j = \begin{pmatrix} \eta_1^j \\ \vdots \\ \eta_N^j \\ \zeta_1^j \\ \vdots \\ \zeta_N^j \\ \chi_1^j \\ \vdots \\ \chi_N^j \\ x_a^j \\ x_b^j \\ x_{h,1}^j \\ \vdots \\ x_{h,W}^j \\ y_a^j \\ y_b^j \end{pmatrix} \quad (\text{B.4})$$

B.2. FD Equations

A list of all FD Equations used during simulation, with shorthand notation

$$f(z_i, t_j) = f_i^j \quad (\text{B.5})$$

Time derivative central FD Equation, to second order accuracy.

$$\frac{\partial f_i^j}{\partial t} = \frac{f_i^{j+1} - f_i^{j-1}}{2\Delta t} + \mathcal{O}(\Delta t^2) \quad (\text{B.6})$$

Time derivative backwards FD Equation, to second order accuracy. Used in mixed time and space damping term.

$$\frac{\partial f_i^j}{\partial t} = \frac{3f_i^j - 4f_i^{j-1} + f_i^{j-2}}{2\Delta t} + \mathcal{O}(\Delta t^2) \quad (\text{B.7})$$

Second spatial derivative central FD Equation, to second order accuracy.

$$\frac{\partial^2 f_i^j}{\partial z^2} = \frac{f_{i+1}^j - 2f_i^j + f_{i-1}^j}{\Delta z^2} + \mathcal{O}(\Delta z^2) \quad (\text{B.8})$$

Fourth spatial derivative central FD Equation, to second order accuracy.

$$\frac{\partial^4 f_i^j}{\partial z^4} = \frac{f_{i+2}^j - 4f_{i+1}^j + 6f_i^j - 4f_{i-1}^j + f_{i-2}^j}{\Delta z^4} + \mathcal{O}(\Delta z^2) \quad (\text{B.9})$$

Time derivative backwards FD Equation, to second order accuracy. Used in v_{rel} for nonlinear friction coefficient calculation and in the frequency dependent damping term, where mixed spatial and time derivatives occur. With this backwards FD Equations, it's possible to solve for f_i^{j+1} in closed form.

$$\frac{\partial f_i^j}{\partial t} = \frac{3f_i^j - 4f_i^{j-1} + f_i^{j-2}}{2\Delta t} + \mathcal{O}(\Delta t^2) \quad (\text{B.10})$$

B.3. FD Operators

Spatial derivative FD operators in matrix notation, with FD coefficients as give in Equations (B.8) and (B.9). They enforce the clamped boundary conditions.

$$\frac{\partial^2}{\partial z^2} = D_{zz} = \begin{pmatrix} -2 & -1 & & & \\ -1 & 2 & -1 & & \\ & \ddots & \ddots & \ddots & \\ & & -1 & 2 & -1 \\ & & & -1 & 2 \end{pmatrix} \quad (\text{B.11})$$

$$\frac{\partial^4}{\partial z^4} = D_{zzzz} = \begin{pmatrix} 6 & -4 & 1 & & & & \\ -4 & 6 & -4 & 1 & & & \\ 1 & -4 & 6 & -4 & 1 & & \\ & \ddots & \ddots & \ddots & \ddots & \ddots & \\ & & 1 & -4 & 6 & -4 & 1 \\ & & & 1 & -4 & 6 & -4 \\ & & & & 1 & -4 & 6 \end{pmatrix} \quad (\text{B.12})$$

B.4. FD Model Equations

Inserting Equations (B.6) to (B.10) in Equations (3.10) and (3.11), we get the entire set of model equations in FD notation. Note that there are $3N + 4 + W$ equations for each state variable Equation (B.4) and W equations for the relative velocity, in total.

B.4.1. Slip

All bow hair and string contact grid points slip ($v_{rel,c} \neq 0$ and $f_i(v_{rel,c}) = \mu(v_{rel,c})f_{b,c}$).

$$\begin{aligned} & \frac{3\eta_c^j - 4\eta_c^{j-1} + \eta_c^{j-2}}{2\Delta t} - a \frac{3\chi_c^j - 4\chi_c^{j-1} + \chi_c^{j-2}}{2\Delta t} \\ & - \left(\frac{3x_b^j - 4x_b^{j-1} + x_b^{j-2}}{2\Delta t} + \frac{3x_{h,c}^j - 4x_{h,c}^{j-1} + x_{h,c}^{j-2}}{2\Delta t} \right) = v_{rel,c} \end{aligned} \quad (\text{B.13a})$$

$$\begin{aligned} & T \frac{\eta_{i+1}^j - 2\eta_i^j + \eta_{i-1}^j}{\Delta z^2} - B \frac{\eta_{i+2}^j - 4\eta_{i+1}^j + 6\eta_i^j - 4\eta_{i-1}^j + \eta_{i-2}^j}{\Delta z^4} - 2b_1 \frac{\eta_i^{j+1} - \eta_i^{j-1}}{2\Delta t} \\ & + b_2 \frac{3\eta_{i+1}^j - 6\eta_i^j + 3\eta_{i-1}^j - 4\eta_{i+1}^{j-1} + 2\eta_i^{j-1} + 8\eta_i^{j-1} - 4\eta_{i-1}^{j-1} + \eta_{i+1}^{j-2} - 2\eta_i^{j-2} + \eta_{i-1}^{j-2}}{\Delta t \Delta z^2} \\ & + f_i(v_{rel,c}) - m \frac{\eta_i^{j+1} - 2\eta_i^j + \eta_i^{j-1}}{\Delta t^2} = 0 \end{aligned} \quad (\text{B.13b})$$

$$\begin{aligned} & T \frac{\zeta_{i+1}^j - 2\zeta_i^j + \zeta_{i-1}^j}{\Delta z^2} - B \frac{\zeta_{i+2}^j - 4\zeta_{i+1}^j + 6\zeta_i^j - 4\zeta_{i-1}^j + \zeta_{i-2}^j}{\Delta z^4} - 2b_1 \frac{\zeta_i^{j+1} - \zeta_i^{j-1}}{2\Delta t} \\ & + b_2 \frac{3\zeta_{i+1}^j - 6\zeta_i^j + 3\zeta_{i-1}^j - 4\zeta_{i+1}^{j-1} + 2\zeta_i^{j-1} + 8\zeta_i^{j-1} - 4\zeta_{i-1}^{j-1} + \zeta_{i+1}^{j-2} - 2\zeta_i^{j-2} + \zeta_{i-1}^{j-2}}{\Delta t \Delta z^2} \\ & - f_{b,i}(\Delta y_{h,c}) - m \frac{\zeta_i^{j+1} - 2\zeta_i^j + \zeta_i^{j-1}}{\Delta t^2} = 0 \end{aligned} \quad (\text{B.13c})$$

$$K \frac{\chi_{i+1}^j - 2\chi_i^j + \chi_{i-1}^j}{\Delta z^2} - 2d_1 \frac{\chi_i^{j+1} - \chi_i^{j-1}}{2\Delta t} - a f_i(v_{rel,c}) - J \frac{\chi_i^{j+1} - 2\chi_i^j + \chi_i^{j-1}}{\Delta t^2} = 0 \quad (\text{B.13d})$$

$$\begin{aligned} & k \left(x_b^j - x_a^j \right) + c \left(\frac{x_b^{j+1} - x_b^{j-1}}{2\Delta t} - \frac{x_a^{j+1} - x_a^{j-1}}{2\Delta t} \right) \\ & + m_g g - w \frac{x_a^{j+1} - x_a^{j-1}}{2\Delta t} - m_a \frac{x_a^{j+1} - 2x_a^j + x_a^{j-1}}{\Delta t^2} = 0 \end{aligned} \quad (\text{B.13e})$$

$$\begin{aligned}
 & -k \left(x_b^j - x_a^j \right) - c \left(\frac{x_b^{j+1} - x_b^{j-1}}{2\Delta t} - \frac{x_a^{j+1} - x_a^{j-1}}{2\Delta t} \right) + k_h \left(x_{h,i}^j - x_b^j \right) \\
 & + c_h \left(\frac{x_{h,i}^{j+1} - x_{h,i}^{j-1}}{2\Delta t} + \frac{x_b^{j+1} - x_b^{j-1}}{2\Delta t} \right) - m_b \frac{x_b^{j+1} - 2x_b^j + x_b^{j-1}}{\Delta t^2} = 0
 \end{aligned} \tag{B.13f}$$

$$\begin{aligned}
 & k_h \left(x_b^j - x_{h,i}^j \right) + c_h \left(\frac{x_b^{j+1} - x_b^{j-1}}{2\Delta t} - \frac{x_{h,i}^{j+1} - x_{h,i}^{j-1}}{2\Delta t} \right) \\
 & + f_i(v_{rel,c}) - m_h \frac{x_{h,i}^{j+1} - 2x_{h,i}^j + x_{h,i}^{j-1}}{\Delta t^2} = 0
 \end{aligned} \tag{B.13g}$$

$$\begin{aligned}
 & k \left(y_a^j - y_b^j \right) + c \left(\frac{y_a^{j+1} - y_a^{j-1}}{2\Delta t} - \frac{y_b^{j+1} - y_b^{j-1}}{2\Delta t} \right) \\
 & - m_b g + \Delta z \sum_{c=e_1}^{e_2} f_{b,c}(\Delta y_{h,c}) - m_b \frac{y_b^{j+1} - 2y_b^j + y_b^{j-1}}{\Delta t^2} = 0
 \end{aligned} \tag{B.13h}$$

B.4.2. Stick

All bow hair and string contact grid points stick ($v_{rel,c} = 0$ and $f(v_{rel}) \in [-\mu_s f_b, \mu_s f_b]$).

During sticking, the friction force $f(v_{rel})$ is determined by the string's restoring force, see Equation (3.10a).

$$f(v_{rel} = 0) = f_{restore} = -T\eta'' + B\eta'''' + 2b_1\dot{\eta} - 2b_2\eta''\dot{\eta} + m\ddot{\eta} \tag{B.14}$$

Thus, in the contact region, $c \in [e_1, \dots, e_2]$, the FD model equations are now given by

$$\begin{aligned}
 & T \frac{\eta_{c+1}^j - 2\eta_c^j + \eta_{c-1}^j}{\Delta z^2} - B \frac{\eta_{c+2}^j - 4\eta_{c+1}^j + 6\eta_c^j - 4\eta_{c-1}^j + \eta_{c-2}^j}{\Delta z^4} - 2b_1 \frac{\eta_c^{j+1} - \eta_c^{j-1}}{2\Delta t} \\
 & + b_2 \frac{3\eta_{c+1}^j - 6\eta_c^j + 3\eta_{c-1}^j - 4\eta_{c+1}^{j-1} + 2\eta_c^{j-1} + 8\eta_c^{j-1} - 4\eta_{c-1}^{j-1} + \eta_{c+1}^{j-2} - 2\eta_c^{j-2} + \eta_{c-1}^{j-2}}{\Delta t \Delta z^2} = f_{restore,c}
 \end{aligned} \tag{B.15a}$$

$$\begin{aligned}
 & \frac{3\eta_i^j - 4\eta_c^{j-1} + \eta_c^{j-2}}{2\Delta t} - a \frac{3\chi_c^j - 4\chi_c^{j-1} + \chi_c^{j-2}}{2\Delta t} \\
 & - \left(\frac{3x_b^j - 4x_b^{j-1} + x_b^{j-2}}{2\Delta t} + \frac{3x_{h,c}^j - 4x_{h,c}^{j-1} + x_{h,c}^{j-2}}{2\Delta t} \right) = 0 = v_{rel,c}
 \end{aligned} \tag{B.15b}$$

Appendix B. Finite Difference Method Implementation

$$T \frac{\zeta_{c+1}^j - 2\zeta_c^j + \zeta_{c-1}^j}{\Delta z^2} - B \frac{\zeta_{c+2}^j - 4\zeta_{c+1}^j + 6\zeta_c^j - 4\zeta_{c-1}^j + \zeta_{c-2}^j}{\Delta z^4} - 2b_1 \frac{\zeta_c^{j+1} - \zeta_c^{j-1}}{2\Delta t} + b_2 \frac{3\zeta_{c+1}^j - 6\zeta_c^j + 3\zeta_{c-1}^j - 4\zeta_{c+1}^{j-1} + 2\zeta_c^{j-1} + 8\zeta_c^{j-1} - 4\zeta_{c-1}^{j-1} + \zeta_{c+1}^{j-2} - 2\zeta_c^{j-2} + \zeta_{c-1}^{j-2}}{\Delta t \Delta z^2} - f_{b,c}(\Delta y_{h,c}) - m \frac{\zeta_c^{j+1} - 2\zeta_c^j + \zeta_c^{j-1}}{\Delta t^2} = 0 \quad (\text{B.15c})$$

$$K \frac{\chi_{c+1}^j - 2\chi_c^j + \chi_{c-1}^j}{\Delta z^2} - 2d_1 \frac{\chi_c^{j+1} - \chi_c^{j-1}}{2\Delta t} - a f_{restore,c} - J \frac{\chi_c^{j+1} - 2\chi_c^j + \chi_c^{j-1}}{\Delta t^2} = 0 \quad (\text{B.15d})$$

$$k(x_b^j - x_a^j) + c \left(\frac{x_b^{j+1} - x_b^{j-1}}{2\Delta t} - \frac{x_a^{j+1} - x_a^{j-1}}{2\Delta t} \right) + m_g g - w \frac{x_a^{j+1} - x_a^{j-1}}{2\Delta t} - m_a \frac{x_a^{j+1} - 2x_a^j + x_a^{j-1}}{\Delta t^2} = 0 \quad (\text{B.15e})$$

$$-k(x_b^j - x_a^j) - c \left(\frac{x_b^{j+1} - x_b^{j-1}}{2\Delta t} - \frac{x_a^{j+1} - x_a^{j-1}}{2\Delta t} \right) + k_h(x_{h,c}^j - x_b^j) + c_h \left(\frac{x_{h,c}^{j+1} - x_{h,c}^{j-1}}{2\Delta t} + \frac{x_b^{j+1} - x_b^{j-1}}{2\Delta t} \right) - m_b \frac{x_b^{j+1} - 2x_b^j + x_b^{j-1}}{\Delta t^2} = 0 \quad (\text{B.15f})$$

$$k_h(x_b^j - x_{h,c}^j) + c_h \left(\frac{x_b^{j+1} - x_b^{j-1}}{2\Delta t} - \frac{x_{h,c}^{j+1} - x_{h,c}^{j-1}}{2\Delta t} \right) + f_{restore,c} - m_h \frac{x_{h,c}^{j+1} - 2x_{h,c}^j + x_{h,c}^{j-1}}{\Delta t^2} = 0 \quad (\text{B.15g})$$

$$k(y_a^j - y_b^j) + c \left(\frac{y_a^{j+1} - y_a^{j-1}}{2\Delta t} - \frac{y_b^{j+1} - y_b^{j-1}}{2\Delta t} \right) - m_b g + \Delta z \sum_{c=e_1}^{e_2} f_{b,c}(\Delta y_{h,c}) - m_b \frac{y_b^{j+1} - 2y_b^j + y_b^{j-1}}{\Delta t^2} = 0 \quad (\text{B.15h})$$

B.5. Matrix Notation

With the state vector from Equation (B.4), we can write Equation (B.13)/(B.15) in matrix form,

$$\mathbf{M}^{j+1}\mathbf{s}^{j+1} + \mathbf{M}^j\mathbf{s}^j + \mathbf{M}^{j-1}\mathbf{s}^{j-1} + \mathbf{M}^{j-2}\mathbf{s}^{j-2} + \mathbf{f} = 0 \quad (\text{B.16})$$

and solve for \mathbf{s}^{j+1} .

$$\begin{aligned} \mathbf{s}^{j+1} &= (\mathbf{M}^{j+1})^{-1}\mathbf{M}^j\mathbf{s}^j + (\mathbf{M}^{j+1})^{-1}\mathbf{M}^{j-1}\mathbf{s}^{j-1} \\ &\quad + (\mathbf{M}^{j+1})^{-1}\mathbf{M}^{j-2}\mathbf{s}^{j-2} + (\mathbf{M}^{j+1})^{-1}\mathbf{f} \end{aligned} \quad (\text{B.17})$$

Simplified with $\mathbf{A}^j = (\mathbf{M}^{j+1})^{-1}\mathbf{M}^j$, $\mathbf{A}^{j-1} = (\mathbf{M}^{j+1})^{-1}\mathbf{M}^{j-1}$, ... the basic time-stepping equation is given by

$$\mathbf{s}^{j+1} = \mathbf{A}^j\mathbf{s}^j + \mathbf{A}^{j-1}\mathbf{s}^{j-1} + \mathbf{A}^{j-2}\mathbf{s}^{j-2} + (\mathbf{M}^{j+1})^{-1}\mathbf{f}. \quad (\text{B.18})$$

The FD matrices \mathbf{A}^j , \mathbf{A}^{j-1} , \mathbf{A}^{j-2} and $(\mathbf{M}^{j+1})^{-1}$ (a separate set each for the slipping and sticking case), contain all model parameters and remain constant during time-stepping, with their coefficients given by Equations (B.13) and (B.15). \mathbf{f} contains all v_{rel} -dependent force terms, calculated with backwards FD Equation (B.10). This allows a relative velocity stick or slip check, prior to the next time step and proceed with the correct (slip or stick) set of matrices.

When simulating finite bow hair width, the hair and string contact region encompasses more than one grid point and partial slipping and sticking situations occur, where the FD matrices \mathbf{A} and $(\mathbf{M}^{j+1})^{-1}$ become a combination of the slipping and sticking case.

A careful comparison of Equation (B.13) and Equation (B.15) yields, that changes occur only for state variables involved with string and hair contact, η_c , χ_c and y_h . Armed with this knowledge, we can define a vector \mathbf{p} , of the same length as \mathbf{s}^j in Equation (B.4), with elements equal to one for all state variable indices involved in sticking contact and zero otherwise. Using *Matlab* code notation, partial slip and stick FD matrices are then given by

$$\begin{aligned} \mathbf{A}_{partial}(\mathbf{p} == 0, :) &= \mathbf{A}_{slip}(\mathbf{p} == 0, :); \\ \mathbf{A}_{partial}(\mathbf{p} == 1, :) &= \mathbf{A}_{stick}(\mathbf{p} == 1, :); \end{aligned} \quad (\text{B.19})$$

Appendix C.

Q-factor and damping coefficients

This section derives the relationship between the transversal and torsional Q-factor and damping coefficients b_1 and d_1 at their respective fundamental frequency.

Guessing a solution

$$\eta = Ae^{-i(kx+\omega t)} \quad (\text{C.1})$$

to the string equation

$$T\eta'' - B\eta'''' - 2b_1\dot{\eta} + 2b_2\eta''\dot{\eta} - m\ddot{\eta} = 0, \quad (\text{C.2})$$

the resulting dispersion relation is given by

$$k^2\left(1 + i\frac{\omega 2b_2}{T}\right) - k^4\frac{B}{T} + i\frac{\omega 2b_1}{T} - \frac{\omega^2}{c^2} = 0, \quad (\text{C.3})$$

with transversal wave speed $c = \sqrt{\frac{T}{m}}$. With the approximations that B is small and $\frac{i\omega 2b_2}{T} \ll 1$ at the fundamental frequency, we get

$$k = \frac{\omega}{c} \sqrt{1 - i\frac{2b_1c^2}{\omega T}}. \quad (\text{C.4})$$

Assuming $\frac{2b_1c^2}{\omega T} \ll 1$ and using Taylor series expansion $\sqrt{1-x} = 1 - \frac{1}{2}x + \mathcal{O}(x^2)$, the dispersion relation for transversal waves at the fundamental frequency, is approximated with reasonable accuracy by

$$k = \frac{\omega}{c} - i\frac{b_1c}{T}. \quad (\text{C.5})$$

Appendix C. Q-factor and damping coefficients

The complex term leads to an exponential decay proportional to $e^{-\frac{\omega}{2Q}t}$. Thus, the transversal quality factor Q_0 of the fundamental frequency ω_0 is determined by

$$Q_0 = \frac{\omega_0 T}{2b_1 c^2}. \quad (\text{C.6})$$

Equivalently, the relationships for torsional waves are given by

$$k = \frac{\omega}{c} - i\frac{d_1 c}{K}, \quad Q_0 = \frac{\omega_0 K}{2d_1 c^2}. \quad (\text{C.7})$$

For large values of Q_0 , the Q-factor approximates the number of oscillations required for the amplitude of a freely oscillating system to drop to $e^{-\pi}$, or 4 % of its initial magnitude.

Appendix D.

Bibliography

- [1] M. Schleske, “On making "tonal copies" of a violin”, *Catgut Acoustical Society Journal* **3**, 18–28 (1996), URL http://www.schleske.de/fileadmin/user/_upload/doc/CAS{}_Tonal{}_Copies.pdf.
- [2] R. Mores, “Precise Cello Bowing Pendulum”, in *Proc. of the 3rd Vienna Talk on Music Acoustics*, 160–161 (2015).
- [3] R. Mores, “Maximum bow force revisited for the cello - Instrumentation with a precision pendulum”, *The Journal of the Acoustical Society of America* **138**, 1888–1888 (2015), URL <https://doi.org/10.1121/1.4960626>.
- [4] C. V. Raman, “Experiments with mechanically-played violins”, *Proceedings of the Indian Association for the Cultivation of Science* **6** (1920).
- [5] K. C. Kar, N. K. Datta, and S. K. Gosh, “Investigation on the Bowed String with an Electrically Driven Bow”, *Indian Journal of Physics* **25**, 423–432 (1951).
- [6] B. Lawergren, “On the Motion of Bowed Violin Strings”, *Acustica* **44**, 194—206 (1980).
- [7] N. Pickering, “A new light of bow action”, *journal of violin society of america* **11**, 83–92 (1991).
- [8] A. Cronhjort, “A computer-controlled bowing machine (MUMS)”, *Speech Trans. Lab. Quarterly Progress and Status* **33**, 061–066 (1992).
- [9] E. Schoonderwaldt, K. Guettler, and A. Askenfelt, “An empirical investigation of bow-force limits in the Schelleng diagram”, *Acta Acustica united with Acustica* **94**, 604–622 (2008).

Appendix D. Bibliography

- [10] W. Vogl, “Bogenstreichmaschine”, Master thesis, Technische Universität Wien (1998).
- [11] P. M. Galluzzo and J. Woodhouse, “High-performance bowing machine tests of bowed-string transients”, *Acta Acustica united with Acustica* **100**, 139–153 (2014).
- [12] A. de Cheveigné and H. Kawahara, “YIN, a fundamental frequency estimator for speech and music”, *The Journal of the Acoustical Society of America* **111**, 1917–1930 (2002), URL <https://doi.org/10.1121/1.1458024>.
- [13] J. M. Grey and J. W. Gordon, “Perceptual effects of spectral modifications on musical timbres”, *The Journal of the Acoustical Society of America* **63**, 1493–1500 (1978), URL <https://doi.org/10.1121/1.381843>.
- [14] J. C. Schelleng, “The bowed string and the player”, *The Journal of the Acoustical Society of America* **53**, 26–41 (1973), URL <http://asa.scitation.org/doi/10.1121/1.1913322>.
- [15] R. Mores, “Complementary empirical data on minimum bow force”, *The Journal of the Acoustical Society of America* **142**, 728–736 (2017), URL <http://asa.scitation.org/doi/10.1121/1.4996141>.
- [16] W. C. Elmore and M. A. Heald, *Physics of Waves* (New York, NY : Dover Publ.) (1985).
- [17] C. A. Coulson and A. Jeffrey, *Waves: A Mathematical Approach to the Common Types of Wave Motion*, 2nd edition (Addison-Wesley Longman Ltd) (1977).
- [18] D. R. Rowland and C. Pask, “The missing wave momentum mystery”, *American Journal of Physics* **67**, 378–388 (1999), URL <https://doi.org/10.1119/1.19272>.
- [19] J. Woodhouse and A. R. Loach, “Torsional Behaviour Of Cello Strings”, *Acta Acustica* **85**, 734–740 (1999).
- [20] N. H. Fletcher and T. D. Rossing, “Nonlinear Effects in Strings”, in *The Physics of Musical Instruments*, second edition, chapter 5.6, 144–148 (Springer) (1997).
- [21] S. Bilbao, “Lossy oscillators”, in *Numerical Sound Synthesis: Finite Difference Schemes and Simulation in Musical Acoustics*, chapter 4.3, 82–86 (JohnWiley & Sons Ltd) (2009).
- [22] J. C. Strikwerda, *Finite Difference Schemes And Partial Differential Equations*, second edition (SIAM) (2004).
- [23] S. Bilbao, *Numerical Sound Synthesis: Finite Difference Schemes and Simulation in Musical Acoustics* (JohnWiley & Sons Ltd) (2009).

- [24] L. Hiller and P. Ruiz, “Synthesizing Musical Sounds by Solving the Wave Equation for Vibrating Objects: Part 1”, *J. Audio Eng. Soc* **19**, 462–470 (1971), URL <http://www.aes.org/e-lib/browse.cfm?elib=2164>.
- [25] L. Hiller and P. Ruiz, “Synthesizing Musical Sounds by Solving the Wave Equation for Vibrating Objects: Part 2”, *J. Audio Eng. Soc* **19**, 542–551 (1971), URL <http://www.aes.org/e-lib/browse.cfm?elib=2156>.
- [26] R. A. Bacon and J. M. Bowsher, “A discrete model of a struck string”, *Acustica* **41**, 21–27 (1978), URL <http://www.ingentaconnect.com/content/dav/aaua/1978/00000041/00000001/art00005>.
- [27] A. Chaigne and A. Askenfelt, “Numerical simulations of piano strings. I. A physical model for a struck string using finite difference methods”, *The Journal of the Acoustical Society of America* **95**, 1112 (1994), URL <https://doi.org/10.1121/1.408459>.
- [28] A. Chaigne and A. Askenfelt, “Numerical simulations of piano strings. II. Comparisons with measurements and systematic exploration of some hammer-string parameters”, *The Journal of the Acoustical Society of America* **95**, 1631–1640 (1994), URL <https://doi.org/10.1121/1.408549>.
- [29] J. Bensa, S. Bilbao, R. Kronland-Martinet, and J. O. Smith, “The simulation of piano string vibration: from physical models to finite difference schemes and digital waveguides.”, *The Journal of the Acoustical Society of America* **114**, 1095–1107 (2003).
- [30] R. Pitteroff and J. Woodhouse, “Mechanics of the Contact Area Between a Violin Bow and a String. Part I: Reflection and Transmission Behaviour”, *Acta Acustica united with Acustica* **84**, 543–562 (1998).
- [31] R. Pitteroff and J. Woodhouse, “Mechanics of the Contact Area Between a Violin Bow and a String. Part II: Simulating the Bowed String”, *Acta Acustica united with Acustica* **84** (1998).
- [32] R. Pitteroff and J. Woodhouse, “Mechanics of the Contact Area Between a Violin Bow and a String. Part III: Parameter Dependence”, *Acta Acustica united with Acustica* **84**, 929–946 (1998).
- [33] C. Desvages and S. Bilbao, “Two-polarisation physical model of bowed strings with non-linear contact and friction forces, and application to gesture-based sound synthesis”, *Applied Sciences* **6**, 1–32 (2016).

Appendix D. Bibliography

- [34] J. H. Smith and J. Woodhouse, “The tribology of rosin”, *Journal of the Mechanics and Physics of Solids* **48**, 1633–1681 (2000).
- [35] H. Mansour, “The bowed string and its playability : Theory, simulation and analysis”, (2016).
- [36] J. Woodhouse, R. T. Schumacher, and S. Garoff, “Reconstruction of bowing point friction force in a bowed string”, *The Journal of the Acoustical Society of America* **108**, 357 (2000).
- [37] E. Maestre, U. Federico, S. Mar, and J. O. S. Iii, “A bowed string physical model including finite-width thermal friction and hair dynamics”, *International Computer Music Conference* (2014), URL <http://mtg.upf.edu/node/3067>.
- [38] H. Mansour, J. Woodhouse, and G. P. Scavone, “Enhanced Wave-Based Modelling of Musical Strings. Part 2: Bowed Strings”, *Acta Acustica united with Acustica* **102**, 1094–1107 (2016), URL <http://openurl.ingenta.com/content/xref?genre=article{%&issn=1610-1928{%&}volume=102{%&}issue=6{%&}spage=1094>.
- [39] F. Fétis, *D’analyses Théoretiques sur l’archet*, in *Antoine Stradivari- Luthiere Célèbre des Instruments a Archet (translated as A Theoretical Analysis of the Bow in Anthony Stadivari: The Celebrated Violin Maker by J. Bishop (Robert Cocks, London, 1864))* (Vuillaume, Paris) (1856), URL <https://play.google.com/store/books/details?id=1S8DAAAQAAJ{%&}rdoc=book-1S8DAAAQAAJ{%&}rdot=1>.
- [40] H. Saint-George, *The Bow, Its History, Manufacture and Use*, third edit edition (HORACE MARSHALL & SON, London, CHARLES CRIBNER’S SONS, New York) (1922).
- [41] M. Kimball, “On making a violin bow”, *Catgut Acoust. Soc. Newsletter* 22–26 (1969).
- [42] O. Reder, “The search for the perfect bow”, *Catgut Acoust. Soc. Newsletter* 21–23 (1970).
- [43] R. T. Schumacher, “Some Aspects of the Bow”, *Catgut Acoust. Soc. Newsletter* 5–8 (1975).
- [44] K. Guettler and A. Askenfelt, “Some aspects of bow resonances - Conditions for spectral influence on the bowed string”, *Stl-Qpsr* **36**, 107–118 (1995), URL <http://www.knutsacoustics.com/files/QPSR--Bow-resonances-1995{ }36{ }2-3{ }107-118.pdf>.

- [45] A. Askenfelt, “Observation on the violin bow and the interaction with the string”, Technical Report, KTH (1995).
- [46] A. Askenfelt, “Observations on the dynamic properties of violin bows”, *Stl-Qpsr* **33**, 043–049 (1992).
- [47] K. H. Hunt and F. R. E. Crossley, “Coefficient of Restitution Interpreted as Damping in Vibroimpact”, *Journal of Applied Mechanics* **42**, 440 (1975).
- [48] J.E. Dennis Jr. and R. B. Schnabel, 6. *Globally Convergent Modifications of Newton’s Method*, 111–154, URL <https://epubs.siam.org/doi/abs/10.1137/1.9781611971200.ch6>.
- [49] O. Inácio, “A Modal Method for the Simulation of Nonlinear Dynamical Systems with Application to Bowed Musical Instruments”, Ph.D. thesis, University of Southampton (2008).